RNF43 mutations facilitate mucinous colorectal cancer metastasis via formation of a tumour-intrinsic niche

Jeroen M. Bugter[1], Layla El Bouazzaoui[1, 2, *], Emre Küçükköse[2, *], Yourae Hong[3], Joep Sprangers[1], Ingrid Jordens[1], Nicola Fenderico[1], Diego Montiel Gonzalez[4], Ruben van Boxtel[4], Saskia J.E. Suijkerbuijk[5], Sabine Tejpar[3], Hugo J.G. Snippert[1], Onno Kranenburg[2, ✉], Madelon M. Maurice[1, ✉]

[1]Oncode Institute and Centre for Molecular Medicine, UMC Utrecht, the Netherlands

[2]Department of Surgical Oncology, Lab Translational Oncology, UMC Utrecht, the Netherlands

[3]Department of Oncology, Katholieke Universiteit Leuven, Belgium

[4]Princes Maxima Centre for Pediatric Oncology, Utrecht, the Netherlands

[5]Division of Developmental Biology, Institute of Biodynamics and Biocomplexity, Department of Biology, Faculty of Science, Utrecht University, The Netherlands.

[*]These authors contributed equally to this work

✉ corresponding authors; email: o.kranenburg@umcutrecht.nl & m.m.maurice@umcutrecht.nl

Abstract

Colorectal cancer (CRC) develops via two mutually exclusive genetic pathways that involve distinct WNT pathway alterations[1–3]. Downstream *APC* mutations initiate development of conventional WNT-high adenocarcinomas. By contrast, *RNF43* mutations induce hypersensitivity to WNTs at the receptor level and are mainly found in BRAF V600E-initiated serrated adenomas that advance into WNT-low mucinous adenocarcinomas with poor prognosis upon metastasis[3–6]. How *RNF43* mutations contribute to tumour progression remains unclear. Here, we employed gene editing to repair *RNF43* mutations in patient-derived CRC organoids. In comparison to their *RNF43*-mutant counterparts, *RNF43*-corrected CRC organoids display a diminished mucinous phenotype, loss of niche factor independency and loss of metastatic capacity upon orthotopic transplantation in mice. Mechanistically, mutant RNF43 promotes formation of a non-dividing secretory cell population that secretes essential growth factors and provide a state of self-sufficiency to the cancer epithelium. Unlike APC mutations, we show that RNF43-mutations provide tuneable WNT levels that permits the formation of these niche-like cells in parallel to proliferative WNT-high cancer cells. Also in patient samples, formation of these tumour-intrinsic niche cells (TINCs) correlate with *RNF43*-mutant CRC, mucinous histology and metastatic capacity and represents a cellular mechanism by which tumours acquire self-sufficiency.

37 **Main**

38 Self-renewal of human colon stem cells is controlled by specialized epithelial and mesenchymal
39 niche cells that secrete essential factors to promote growth and prevent differentiation[7].
40 Different from healthy adult colon stem cells, patient-derived CRC cells commonly display loss
41 of niche factor-dependency during *in vitro* outgrowth into organoids (Extended Data Fig. 1a),
42 which correlates with their metastatic capacity *in vivo*[8,9]. While *APC*-mutant CRC organoids
43 typically display WNT-independent growth, *RNF43/BRAF*-mutant CRC organoids are
44 sensitive to Porcupine inhibition, indicating their growth depends on self-produced WNT
45 ligands (Extended Data Fig. 1b)[9,10]. Despite their dependence on WNTs, *RNF43/BRAF*-mutant
46 CRC organoids are characterized by relatively low levels of WNT target gene expression and
47 an increased expression of mucin-related genes (Extended Data Fig. 1c).

48 To address the functional driver role of mutated *RNF43*, we employed the
49 *RNF43/BRAF*-mutant human CRC organoid line (HUB040; Extended Data Fig. 1) derived
50 from a primary human mucinous colorectal adenocarcinoma that presented with prominent
51 metastasis in the patient[11]. We employed gene editing to correct the mutated *RNF43* locus to
52 wildtype and obtained two *RNF43*-corrected clones (RC1, RC2) and one non-corrected control
53 clone (NC1) (Fig. 1a, b). Whole genome sequencing of all clones confirmed preservation of
54 pre-existing HUB040 driver mutations, other than *RNF43* (Extended Data Fig. 2a). Karyotypes
55 of HUB040, NC1 and RC2 were similar, while RC1 was somewhat divergent, mainly due to
56 whole genome duplication (Extended Data Fig. 2b-g). To investigate metastatic capacity, we
57 performed orthotopic transplantation of organoids into the caecal wall of immune-deficient
58 mice[12]. After 120 days, HUB040 and NC1 had formed primary tumours that spontaneously
59 metastasized to the lungs and the liver (Fig. 1c, d, Extended Data Fig. 3a). Strikingly, for
60 transplanted *RNF43*-corrected organoids no metastatic lesions were detected (Fig. 1c, d), even
61 though their primary tumour load equalled that of *RNF43*-mutant counterparts (Extended Data

62 Fig. 3a). Thus, by restoring a single mutation we eliminated the metastatic capacity of this
63 aggressive cancer model. These data suggest a key role for mutated *RNF43* in promoting
64 metastasis.

65 Next, we assessed organoid niche-independency by performing single cell
66 reconstitution assays in growth factor-depleted conditions. Like HUB040, *RNF43*-mutant NC1
67 organoids retained their capacity to expand in medium lacking extrinsic growth factors (Fig.
68 1e, Extended Data Fig. 3b-d). By contrast, *RNF43*-repaired lines RC1 and RC2 acquired a
69 strong dependence on supplementation with WNT, RSPO and EGF (Fig. 1e, Extended Data
70 Fig. 3b-d). These results were unexpected, as introduction of *RNF43* mutations in healthy
71 human colon-derived or mouse intestinal organoids are known to enhance WNT sensitivity[6],
72 but are not known to alter EGF dependency. Our data thus imply a role for *RNF43* mutations
73 in promoting cancer cell survival and growth in the absence of growth factor supplementation.

74 We next aimed to investigate how *RNF43* mutations affect tumour phenotype.
75 Transcriptome comparison of HUB40, NC1 and both RC organoid lines yielded a mutant
76 *RNF43*-driven gene expression signature that comprised numerous genes encoding growth
77 factors and mucins (Fig. 2a, b, Extended Data Fig. 4a, b). In line with these findings, gene sets
78 representing Goblet and Deep Crypt Secretory (DCS) cells of healthy colon were significantly
79 depleted from RC1 and RC2 in comparison to control lines (Fig. 2c)[13,14]. Furthermore, *RNF43*-
80 mutant tumours displayed extensive mucus secretion *in vitro* and *in vivo*, while this property
81 was strongly diminished upon *RNF43* correction (Fig. 2d-f), strengthening the observation that
82 *RNF43* mutations facilitate secretory cell differentiation.

83 Notably, the *RNF43*-mutant signature comprised several reported niche factors
84 including *IGF2*, *VEGFA*, *DLL1*/*4* and *WNT8B* (Fig. 2a, b, Extended Data Fig. 4b). Blocking
85 upstream IGF and WNT signalling diminished reconstitution capacity of HUB40 CRC
86 organoids, which was rescued by supplementation with exogenous EGF or WNT ligands,

respectively (Fig. 2g, h), reminiscent of the growth state of *RNF43*-corrected organoids (Fig. 1e, Extended Data Fig. 3b-d). Based on these data, we hypothesized that *RNF43* mutations accommodate the production of self-produced niche-factors that are essential for tumour survival and growth. To test this, we generated hybrid co-cultures of *RNF43*-mutant and *RNF43*-corrected organoids and monitored them over time in growth factor-depleted medium using live imaging (Fig 2i, Supplementary Videos 1-2)[15]. While cultures of unmixed *RNF43*-corrected organoids displayed a high ratio of cell death over mitotic events, this ratio was reversed when *RNF43*-corrected cells shared a lumen with *RNF43*-mutant cells (Fig 2j). These results confirm that HUB040 CRC survival relies on paracrine signalling events that are facilitated by mutant RNF43.

In a previous study, we showed that inactivation of *Rnf43* and its paralogue *Znrf3* in the mouse small intestine induces hyperplasia of stem cells as well as secretory Paneth cells, that function as an intra-epithelial stem cell niche[16,17]. To investigate how *RNF43* mutations may promote the formation of specialized niche factor-producing cells within human CRC, we first performed single cell RNA sequencing analysis of the HUB040 organoid line. Single cell profiles spanned seven clusters with distinct expression patterns discovered by unsupervised clustering (Fig. 3a, Extended Data Fig. 5a). Noticeably, one population of cells (cluster 1), representing about one-sixth of tumour cells, entirely lacked expression of proliferation and stem cell-related genes[18] (Fig. 3b, c, Extended Data Fig. 5b). Instead, this subset displayed prominent hallmarks of differentiated secretory niche cells, as exemplified by the expression of gene sets related to Goblet cells (Fig. 3d), Deep Crypt Secretory (DCS) cells (Fig. 3e)[13,14], hypoxia and glycolysis (Extended Data Fig. 5c-e)[19,20], as well as mTOR activation and the unfolded protein response (Extended Data Fig. 5e)[21–23]. We thus identified cluster 1 as a non-proliferating, niche factor-producing secretory cancer cell subset that we call tumour-intrinsic niche cells (TINCs).

112 Subjection of healthy colon organoids to growth factor depletion caused emergence of
113 a TINC and DCS signature-enriched cell population, supporting the observation that TINCs
114 share identity with differentiated, healthy DCS cells (Extended Data Fig. 6)[13]. Notably, the
115 TINC gene signature was significantly downregulated in both RNF43-corrected clones
116 (Extended Data Fig. 5f). scRNAseq analysis of all clones in complete medium revealed that
117 16% of both HUB040 and NC1 cells displayed high expression of the full TINC signature
118 which was reduced to 1-7% of cells within RNF43-corrected clones (Fig. 3f). In agreement,
119 expression of prominent TINC markers was diminished in RNF43-corrected clones (Fig. 3g).
120 Based on these findings, we conclude that TINC formation is promoted by mutant RNF43.
121 To characterise mutant *RNF43*-dependent TINC cells, we focussed on *NDRG1*, that we
122 identified as a prominent marker gene for TINCs in HUB40 organoids, and for DCS cells in
123 healthy colon organoids (Extended Data Fig. 5g, Extended Data Fig. 6i). Introduction of an
124 IRES-linked mNeon green fluorophore within the *NDRG1* gene revealed that TINCs are
125 heterogeneously distributed within HUB040 (Fig. 3h, i, Extended Data Fig. 7a). Non-dividing
126 NDRG1^{high} TINC reporter cells were interspersed with proliferative NDRG1^{low} cells as shown
127 by KI67 labelling (Fig. 3i) and EdU incorporation (Fig. 3j). Despite their differentiated and
128 non-proliferative appearance, TINCs retained regenerative capacity, as isolated NDRG1^{high},
129 NDRG1^{medium} and NDRG1^{low} single cells gave rise to fully grown organoids in which the
130 heterogeneous distribution of TINCs was restored (Fig. 3k, Extended Data Fig. 7b). Our data
131 thus reveal that *RNF43/BRAF*-mutant HUB040 CRC organoids display phenotypic
132 heterogeneity and are capable of self-organising into a mixture of non-proliferative TINCs and
133 stem-like cell populations.
134 An in-depth transcriptome characterization of sorted NDRG1^{high} cells compared to
135 sorted NDRG1^{medium} and NDRG1^{low} cells (Extended Data Fig. 7c-e) generated an 'extended
136 TINC signature' of about 1.000 genes that robustly confirmed previously identified TINC

137 hallmarks (Extended Data Fig. 7f, g, 5e), including mutant *RNF43*-dependent niche factors such
138 as *IGF2, Dll1, IGFBP2* and *VEGFA* (Fig. 3l, m). Intriguingly, TINCs displayed a relatively
139 decreased expression of WNT target genes, including *RNF43* itself (Fig. 3m). These results
140 support a model in which *RNF43* mutations allow for tuneable WNT signalling and intra-
141 tumoural lineage diversification, even though all cells are *RNF43*-mutant. Lastly, marker genes
142 related to regeneration (*ANXA1*) and metastatic relapse (*EMP1*) were enriched in TINCs (Fig.
143 3m)[24,25]. We conclude that *RNF43* mutations facilitate tumour cell differentiation into niche
144 factor-producing cells, which explains the acquired niche-independent growth state of these
145 tumours.

146 We next explored the broader relevance of TINCs for human CRC. TINC marker gene
147 expression was significantly enriched in *RNF43*-mutant as well as mucinous CRC subtypes of
148 the cancer genomics atlas (TCGA) (Fig. 4a, b). Moreover, TINC gene expression was
149 significantly enhanced in lung and liver metastases compared to primary colorectal tumours
150 (Fig. 4c, Extended Data Fig. 8a). At the single cell level, CRC tumours were recently classified
151 into two intrinsic epithelial subtypes[1]. Among these, TINC signature expression was highest in
152 the iCMS3 group, in which *RNF43* mutations are predominantly found (Fig. 4d)[1]. Furthermore,
153 within iCMS3 tumours, TINC signature expression was higher in *RNF43*-mutant compared to
154 *RNF43* wildtype cases (Fig. 4d). We corroborated these findings by re-analysis of 18.320 single
155 cell transcriptomes derived from CRC tumours of 28 patients, of which four were *RNF43*
156 mutant[1] (Extended Data Fig. 8d). Supervised clustering with batch correction resolved eight
157 shared CRC cell clusters. In comparison with *RNF43* wildtype CRC, *RNF43*-mutant CRC
158 accumulated a larger fraction of cells within two clusters (cluster 3 and 5) (Fig. 4e, f, Extended
159 Data Fig. 8e) that were enriched for *RNF43*-regulated genes (Extended Data Fig. 8g).
160 Additionally, cluster 5 was enriched for goblet cell markers, while TINC markers mapped to
161 cluster 3, exemplified by high *NDRG1* expression (Fig. 4g, Extended Data Fig. 8g). Thus,

162 *RNF43*-mutant CRC subsets are not only enriched for TINC marker expression but also display
163 an overall increased fraction of TINCs (Extended Data Fig 8f).

164 The fraction of TINCs was lowest in iCMS2 subgroups that is often driven by *APC*
165 mutations and high WNT signalling (Fig. 4d)[1]. In line, TINC marker gene expression inversely
166 correlated with high WNT signalling and *APC* mutations when analysed in TCGA (Extended
167 Data Fig. 8b, c). To investigate how *APC* mutations affect WNT signalling and TINC formation
168 in context of a non-iCMS2 tumour, we introduced a conventional truncating mutation in the
169 *APC* mutation cluster region of the HUB040 organoid. Surprisingly, and in contrast to healthy
170 colon organoids[26], biallelic targeting of *APC* was rather inefficient in HUB040 (Extended Data
171 Fig. 9a), in line with the observed mutual exclusivity of *APC* mutations in *BRAF/RNF43*-mutant
172 human cancers[27]. Compared to HUB040$^{APC+/-}$ clones that we obtained, HUB040$^{APC-/-}$ organoid
173 clones displayed prominent WNT/β-catenin target gene expression, enhanced nuclear β-catenin
174 levels and acquired resistance to treatment with WNT secretion inhibitors (Fig. 5a, b Extended
175 Data Fig. 9b-d). Furthermore, introduction of truncated APC induced enrichment of gene
176 signatures representing transit amplifying (TA) cells and stem-like cells, while secretory cell
177 profiles and the TINC signature were significantly reduced (Fig 5c, d)[28]. Single cell analysis
178 revealed that introduction of an *APC* mutation shifted HUB040 cell identity and composition,
179 as shown by an increased fraction of WNT-high cells and a reduced fraction of cells expressing
180 the TINC signature (Fig. 5e, f, Extended Data Fig. 9e-g). These alterations were not compatible
181 with efficient growth, as HUB040$^{APC-/-}$ organoids were outcompeted by HUB040^{APCwt}
182 organoids during co-culture (Fig. 5g). We conclude that *APC* mutations, in context of a
183 *BRAF/RNF43*-mutant tumour background, interfere with intra-epithelial niche formation that
184 is otherwise facilitated by mutant *RNF43*.

185 We hypothesized that adjustable levels of WNT signalling are vital for *BRAF/RNF43*-
186 mutant tumour self-organising capacity. Indeed, constitutive pharmacological activation of

187 WNT signalling (CHIR99021) was not tolerated by HUB040 organoids (Fig. 5h). Furthermore,
188 HUB040 organoids treated with WNT inhibitors for 24 and 48 hours (Extended Data Fig. 9h-
189 j) revealed an incremental downregulation of proliferative, stem and TA signatures and an
190 increase in differentiation signatures, including TINC (Fig. 5c, d). In line with these findings,
191 the number and brightness of TINC reporter cells in HUB040 increased upon WNT inhibitor
192 treatment (Fig. 5i, Extended Data Fig. 9k). Thus, although *BRAF/RNF43*-mutant mucinous
193 cancers are wired towards lower levels of WNT signalling that are optimal to facilitate secretory
194 differentiation, a threshold of WNT signalling in a subset of cancer cells is still required to
195 prevent terminal differentiation and maintain self-renewal of proliferative cells (Fig. 5j).

196 Self-organisation principles are known to promote tumour progression in CRC[29–36], but
197 thus far the underlying genetic driver events remained poorly understood. In this study, we
198 show that *RNF43* mutations facilitate the generation of tumour-intrinsic NDRG1^{high}/VEGFA^{high}
199 secretory niche cells. Different from classical *APC* mutations that promote uniform high WNT
200 signalling in all tumour cells, *RNF43* mutations allow tuneable WNT activity to drive a growth
201 state that relies on interactions between dividing and non-dividing cancer cell populations (Fig.
202 5k). This role of mutated *RNF43* is reminiscent of the concomitant hyperplasia of stem cells
203 and Paneth cells induced by co-deletion of *Rnf43/Znrf3* from the mouse small intestine[16]. In
204 human colon cancer development, however, *RNF43* mutations arise after tumour-initiating
205 *BRAF* mutations[3,6,27]. Consistently, our results indicate that *RNF43* mutations are crucial for
206 metastatic spread, but not for tumour initiation. As niche-independency correlates with
207 metastatic capacity in CRC[9], it is tempting to speculate that induced TINC formation is a
208 prerequisite for metastasis to distant organs. In line with this assumption, recent work has
209 uncovered phenotypic plasticity as a hallmark of CRC metastasis[33,35,36]. While we reveal a key
210 role of adjustable WNT signalling for TINC formation and *BRAF*/*RNF43*-mutant tumour
211 survival and growth, additional pathways may play a role. *RNF43* truncating mutations were

212 recently linked to activation of the PI3K-Akt-mTOR pathway[37], which also mediates activation
213 of cellular programs linked to glycolysis and hypoxia[38], as well as Goblet and Paneth cell
214 differentiation in the mouse intestine and human intestinal organoids[22,23,39,40]. Our findings
215 further indicate that the cancer driver activity of WNT mutations relies on a specific mutational
216 context. Additionally, we found that *RNF43* mutations are causative to a mucinous CRC
217 phenotype. How excessive mucus production links to cancer development and metastasis
218 formation remains incompletely understood[41], although roles in immune evasion, growth factor
219 trapping and chemoprotection were proposed[42]. Thus, our observations likely have wider
220 implications for other *RNF43*-mutant cancers with mucinous histology, including intraductal
221 mucinous carcinoma of the pancreas and mucinous ovarian cancer[43–45]. Our study demonstrates
222 that genetic correction of putative driver genes in patient-derived organoids is a powerful
223 approach to examine the mechanistic role of these mutations in an advanced human cancer
224 context.
225

226 **References**

227 1. Joanito, I. *et al.* Single-cell and bulk transcriptome sequencing identifies two epithelial
228 tumor cell states and refines the consensus molecular classification of colorectal
229 cancer. *Nat. Genet.* **54**, 963–975 (2022).

230 2. Nguyen, L. H., Goel, A. & Chung, D. C. Pathways of Colorectal Carcinogenesis.
231 *Gastroenterology* **158**, 291–302 (2020).

232 3. Chen, B. *et al.* Differential pre-malignant programs and microenvironment chart
233 distinct paths to malignancy in human colorectal polyps. *Cell* **184**, 6262-6280.e26
234 (2021).

235 4. Bugter, J. M., Fenderico, N. & Maurice, M. M. Mutations and mechanisms of WNT

236 pathway tumour suppressors in cancer. *Nat. Rev. Cancer* **21**, 5–21 (2021).

237 5. McCarthy, A. J., Serra, S. & Chetty, R. Traditional serrated adenoma: an overview of
238 pathology and emphasis on molecular pathogenesis. *BMJ Open Gastroenterol.* **6**,
239 e000317 (2019).

240 6. Yan, H. H. N. N. *et al.* RNF43 germline and somatic mutation in serrated neoplasia
241 pathway and its association with BRAF mutation. *Gut* **66**, 1645–1656 (2017).

242 7. Spit, M., Koo, B. K. & Maurice, M. M. Tales from the crypt: Intestinal niche signals in
243 tissue renewal, plasticity and cancer. *Open Biol.* **8**, (2018).

244 8. Fumagalli, A. *et al.* Genetic dissection of colorectal cancer progression by orthotopic
245 transplantation of engineered cancer organoids. *Proc. Natl. Acad. Sci. U. S. A.* **114**,
246 E2357–E2364 (2017).

247 9. Fujii, M. *et al.* A Colorectal Tumor Organoid Library Demonstrates Progressive Loss
248 of Niche Factor Requirements during Tumorigenesis. *Cell Stem Cell* **18**, 827–838
249 (2016).

250 10. Van De Wetering, M. *et al.* Prospective derivation of a living organoid biobank of
251 colorectal cancer patients. *Cell* **161**, 933–945 (2015).

252 11. Ubink, I. *et al.* Organoids from colorectal peritoneal metastases as a platform for
253 improving hyperthermic intraperitoneal chemotherapy. *Br. J. Surg.* **106**, 1404–1414
254 (2019).

255 12. Fumagalli, A. *et al.* A surgical orthotopic organoid transplantation approach in mice to
256 visualize and study colorectal cancer progression. *Nat. Protoc.* **13**, 235–247 (2018).

257 13. Sasaki, N. *et al.* Reg4+ deep crypt secretory cells function as epithelial niche for Lgr5+
258 stem cells in colon. *Proc. Natl. Acad. Sci. U. S. A.* **113**, E5399–E5407 (2016).

259 14. Wang, Y. *et al.* Single-cell transcriptome analysis reveals differential nutrient
260 absorption functions in human intestine. *J. Exp. Med.* **217**, (2020).

261 15. Krotenberg Garcia, A., van Rheenen, J. & Suijkerbuijk, S. J. E. Generation of mixed
262 murine organoids to model cellular interactions. *STAR Protoc.* **2**, 100997 (2021).

263 16. Koo, B. K. *et al.* Tumour suppressor RNF43 is a stem-cell E3 ligase that induces
264 endocytosis of Wnt receptors. *Nature* **488**, 665–669 (2012).

265 17. Sato, T. *et al.* Paneth cells constitute the niche for Lgr5 stem cells in intestinal crypts.
266 *Nature* **469**, 415–418 (2011).

267 18. Oost, K. C. *et al.* Specific Labeling of Stem Cell Activity in Human Colorectal
268 Organoids Using an ASCL2-Responsive Minigene. *Cell Rep.* **22**, 1600–1614 (2018).

269 19. Rodríguez-Colman, M. J. *et al.* Interplay between metabolic identities in the intestinal
270 crypt supports stem cell function. *Nature* **543**, 424–427 (2017).

271 20. Glover, L. E., Lee, J. S. & Colgan, S. P. Oxygen metabolism and barrier regulation in
272 the intestinal mucosa. *J. Clin. Invest.* **126**, 3680–3688 (2016).

273 21. Huang, J. *et al.* Unfolded protein response in colorectal cancer. *Cell Biosci.* **11**, 1–16
274 (2021).

275 22. Sampson, L. L., Davis, A. K., Grogg, M. W. & Zheng, Y. MTOR disruption causes
276 intestinal epithelial cell defects and intestinal atrophy postinjury in mice. *FASEB J.* **30**,
277 1263–1275 (2016).

278 23. He, G. *et al.* Optimized human intestinal organoid model reveals interleukin-22-
279 dependency of paneth cell formation. *Cell Stem Cell* 1–13 (2022).
280 doi:10.1016/j.stem.2022.08.002

281 24. Cañellas-Socias, A. *et al.* Metastatic recurrence in colorectal cancer arises from
282 residual EMP1+ cells. *Nature* (2022). doi:10.1038/s41586-022-05402-9

283 25. Vasquez, E. G. *et al.* Dynamic and adaptive cancer stem cell population admixture in
284 colorectal neoplasia. *Cell Stem Cell* **29**, 1213-1228.e8 (2022).

285 26. Drost, J. *et al.* Sequential cancer mutations in cultured human intestinal stem cells.
286 *Nature* **521**, 43–47 (2015).

287 27. Giannakis, M. *et al.* RNF43 is frequently mutated in colorectal and endometrial
288 cancers. *Nat. Genet.* **46**, 1264–1266 (2014).

289 28. Michels, B. E. *et al.* Human colon organoids reveal distinct physiologic and oncogenic
290 Wnt responses. *J. Exp. Med.* **216**, 704–720 (2019).

291 29. Uhlitz, F. *et al.* Mitogen-activated protein kinase activity drives cell trajectories in
292 colorectal cancer. *EMBO Mol. Med.* **13**, 1–17 (2021).

293 30. Miller, S. A. *et al.* LSD1 and aberrant DNA methylation mediate persistence of
294 enteroendocrine progenitors that support BRAF-mutant colorectal cancer. *Cancer Res.*
295 **81**, 3791–3805 (2021).

296 31. Shimokawa, M. *et al.* Visualization and targeting of LGR5+ human colon cancer stem
297 cells. *Nature* **545**, 187–192 (2017).

298 32. Morral, C. *et al.* Zonation of Ribosomal DNA Transcription Defines a Stem Cell
299 Hierarchy in Colorectal Cancer. *Cell Stem Cell* **26**, 845-861.e12 (2020).

300 33. Sacchetti, A. *et al.* Phenotypic plasticity underlies local invasion and distant metastasis
301 in colon cancer. *Elife* **10**, 1–28 (2021).

302 34. Van Der Heijden, M. *et al.* Spatiotemporal regulation of clonogenicity in colorectal

303 cancer xenografts. *Proc. Natl. Acad. Sci. U. S. A.* **116**, 6140–6145 (2019).

304 35. Fumagalli, A. *et al.* Plasticity of Lgr5-Negative Cancer Cells Drives Metastasis in
305 Colorectal Cancer. *Cell Stem Cell* **26**, 569-578.e7 (2020).

306 36. Heinz, M. C. *et al.* Liver Colonization by Colorectal Cancer Metastases Requires YAP-
307 Controlled Plasticity at the Micrometastatic Stage. *Cancer Res.* **82**, 1953–1968 (2022).

308 37. Fang, L. *et al.* RNF43 G659fs is an oncogenic colorectal cancer mutation and sensitizes
309 tumor cells to PI3K/mTOR inhibition. *Nat. Commun.* **13**, 1–12 (2022).

310 38. Hoxhaj, G. & Manning, B. D. The PI3K–AKT network at the interface of oncogenic
311 signalling and cancer metabolism. *Nat. Rev. Cancer* **20**, 74–88 (2020).

312 39. Zhou, Y., Rychahou, P., Wang, Q., Weiss, H. L. & Evers, B. M. TSC2/mTORC1
313 signaling controls Paneth and goblet cell differentiation in the intestinal epithelium.
314 *Cell Death Dis.* **6**, 1–10 (2015).

315 40. Araujo, A. *et al.* IFN-γ mediates Paneth cell death via suppression of mTOR. *Elife* **10**,
316 1–19 (2021).

317 41. Hugen, N., Brown, G., Glynne-Jones, R., De Wilt, J. H. W. & Nagtegaal, I. D.
318 Advances in the care of patients with mucinous colorectal cancer. *Nat. Rev. Clin.*
319 *Oncol.* **13**, 361–369 (2016).

320 42. Kufe, D. W. Mucins in cancer: function, prognosis and therapy. *Nat. Rev. Cancer* **9**,
321 874–885 (2009).

322 43. Ryland, G. L. *et al.* RNF43 is a tumour suppressor gene mutated in mucinous tumours
323 of the ovary. *J. Pathol.* **229**, 469–476 (2013).

324 44. Lee, J. H., Kim, Y., Choi, J. W. & Kim, Y. S. KRAS, GNAS, and RNF43 mutations in

325 intraductal papillary mucinous neoplasm of the pancreas: a meta-analysis. *Springerplus*
326 **5**, (2016).

327 45. Sakamoto, H. *et al.* Clinicopathological significance of somatic RNF43 mutation and
328 aberrant expression of ring finger protein 43 in intraductal papillary mucinous
329 neoplasms of the pancreas. *Mod. Pathol.* **28**, 261–267 (2015).

330

331 **Figures**

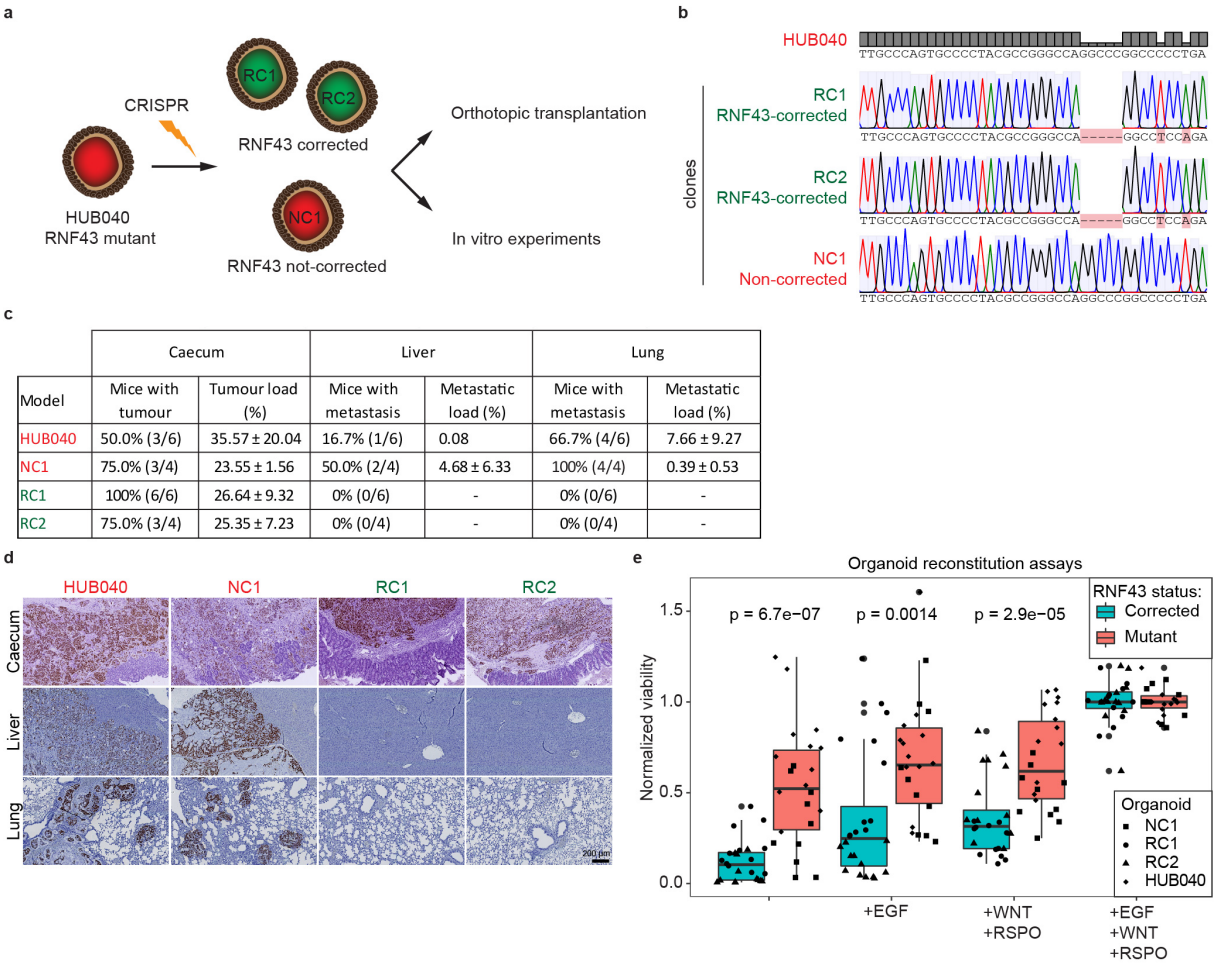

	Caecum		Liver		Lung	
Model	Mice with tumour	Tumour load (%)	Mice with metastasis	Metastatic load (%)	Mice with metastasis	Metastatic load (%)
HUB040	50.0% (3/6)	35.57 ± 20.04	16.7% (1/6)	0.08	66.7% (4/6)	7.66 ± 9.27
NC1	75.0% (3/4)	23.55 ± 1.56	50.0% (2/4)	4.68 ± 6.33	100% (4/4)	0.39 ± 0.53
RC1	100% (6/6)	26.64 ± 9.32	0% (0/6)	-	0% (0/6)	-
RC2	75.0% (3/4)	25.35 ± 7.23	0% (0/4)	-	0% (0/4)	-

332

333 **Fig. 1 | Restoring *RNF43* mutations in patient derived organoids prevents metastasis and**
334 **niche-independent outgrowth. a.** Schematic of experimental setup of this study. **b.** Sanger
335 sequencing traces of *RNF43*-corrected clones (RC1, RC2) and non-corrected control clone
336 (NC1) compared to the locus of the HUB040 CRC organoid. **c.** Table showing tumour forming
337 efficiency and tumour/metastatic load in caecum, liver and lung, 120 days after transplantation.
338 Tumour and metastatic load were determined as human nucleoli area over total tissue area. **d.**
339 Representative human nucleoli stainings of caecum, lung and liver of mice, 120 days after
340 transplantation of indicated HUB040 clones. Scale bar = 200 µm **e.** Normalized viability of
341 *RNF43* mutant and *RNF43*-corrected HUB040 clones treated as in Extended Data Fig. 3b, c.
342 Results of six experiments are presented, including one to three replicates per condition per
343 experiment (n =12 per condition in total). Data are normalised against mean value in complete

344 medium per experiment. Kruskal-Wallis test is used to compare *RNF43* mutant and corrected

345 within each condition.

346

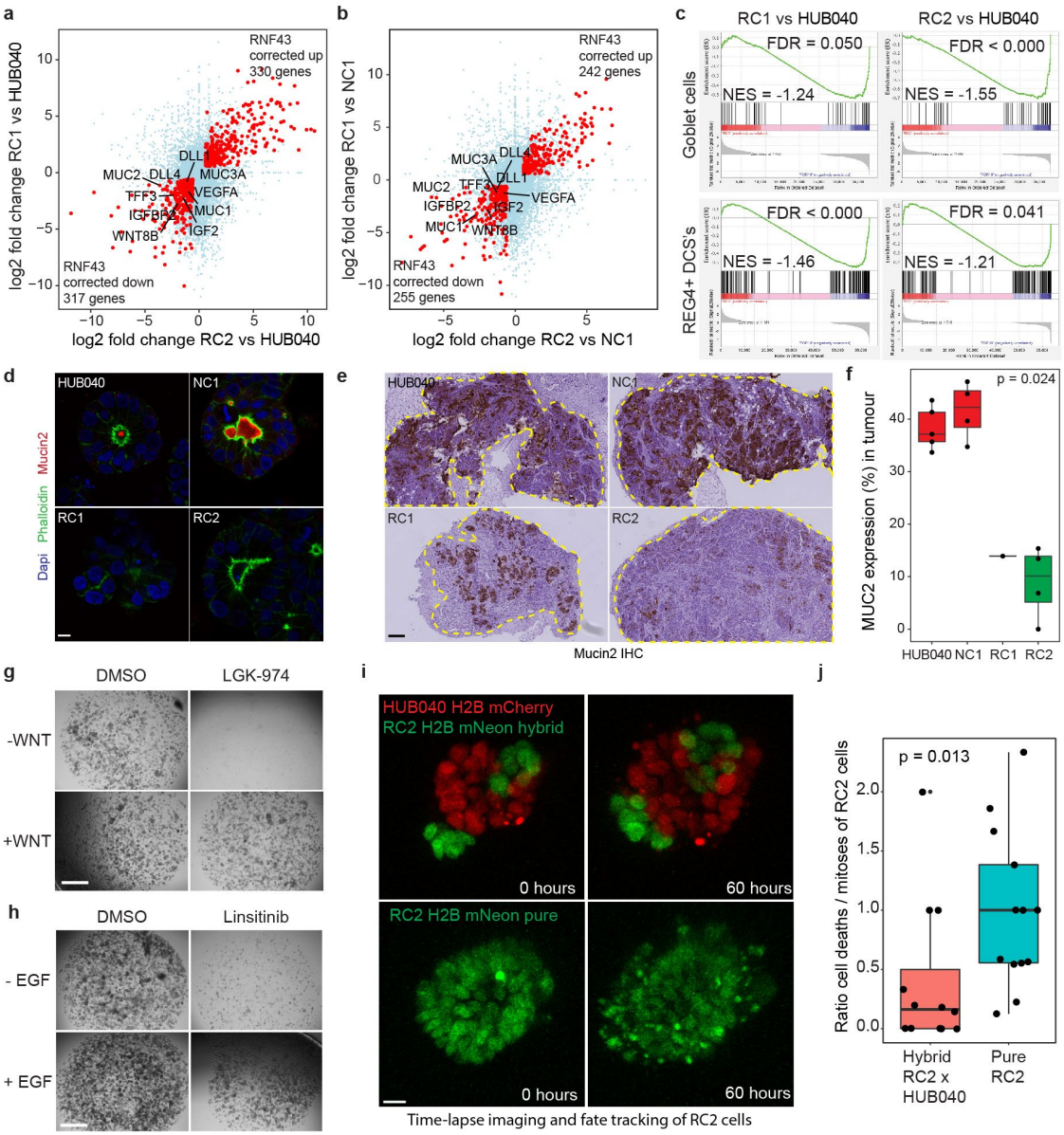

347

348 **Fig. 2 | *RNF43* mutation drives mucinous differentiation and niche factor production. a,**

349 **b.** Scatter plots showing log2 fold change of gene expression between *RNF43*-corrected clones,

350 RC1 (Y-axis) and RC2 (X-axis), and HUB040 (**a**) or non-corrected clone 1 (NC1) (**b**). Genes

351 with significant differential expression (FC > 1.5 and $p < 0.05$) in both comparisons are

352 indicated as larger red dots. Downregulated genes of interest are annotated. Total number of

genes that are up- or downregulated in both comparisons is plotted in the corners. **c.** GSEA plots showing enrichment of a colonic goblet cell signature[14] and REG4+ deep crypt secretory cell (DCS) signature[13] in HUB040 compared to RC1 or RC2. **d.** Representative confocal microscopy images of organoids stained for mucin2 (MUC2, in red), actin (phalloidin, green) and nuclei (dapi, blue). Scale bar = 10 µm. **e.** Representative IHC images for mucin2 (MUC2) on primary subcutaneous tumours. Scale bar = 250 µm. **f.** Box plots showing the percentage of MUC2+ tumour area in primary subcutaneous tumours. Significance was evaluated using a Krusak-Wallis test. **g, h.** Representative low-magnification brightfield images of HUB040 organoids treated with 100 nM PORCN inhibitor LGK-974 (**g**), 1 µM IR/IGFR inhibitor Linsitinib (**h**) or DMSO in CRC culture medium with or without WNT surrogate (**g**) or EGF (**h**) supplementation for 14 days, passaged after 7 days. Scale bar = 1000 µm. **i.** Representative 3D projected images of time-lapse series of hybrid HUB040-RC2 or pure RC2 organoids in CRC medium at the start and end of the time-lapse; nuclei are visualized by expression of H2B-mNeon or H2B-mCherry. Scale bar represent 20 µm. **j.** Result of analysis of RC2-cell fate over time in the two conditions. Cell death and mitotic events were counted for all RC2-H2B-mNeon cells in 13-14 movies per condition. The ratio of number of cell death over mitotic events is shown.

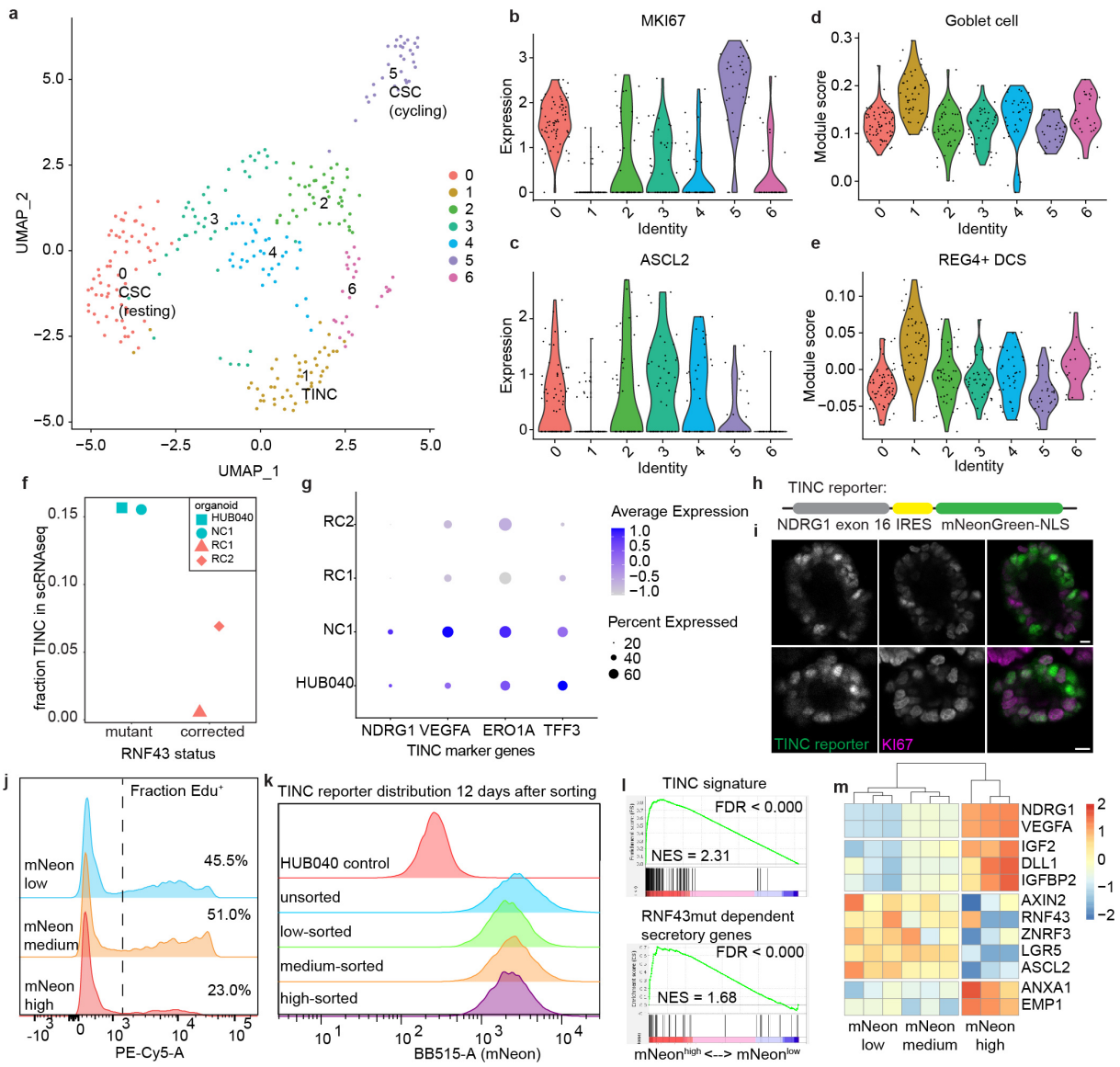

Fig. 3 | *RNF43* mutation promotes tumour-intrinsic niche cell formation. a. Reduced dimensionality (UMAP) visualisation of single cell RNA sequencing data of HUB040 organoids cultured in CRC medium. Results of unsupervised clustering are colour-coded per cluster. **b, c.** Violin plots showing scaled single cell expression levels of proliferation marker MKI67 (**b**) and cancer stem-cell marker ASCL2 (**c**) grouped by cluster. **d, e.** Violin plots showing single cell module scores for expression of genes from a colonic goblet cell signature[14] (**d**) and REG4+ deep crypt secretory cell (DCS) signature[13] (**e**) grouped by cluster. **f.** Plot showing the fraction of cells that were scored as TINC in the analysis of single cell RNA sequencing data of the four indicated organoid lines. **g.** Dot-plot showing the average

381 expression and fraction of cells expressing indicated TINC marker genes. **h.** Schematic of the
382 endogenous TINC reporter construct. **i.** Representative confocal microscopy pictures of TINC
383 reporter-positive cells (mNeon) in HUB040 organoids, combined with KI67 immunostaining.
384 Scale bar = 10 µm. **j.** FACS plot of HUB040 TINC reporter organoids gated for low, medium
385 or high mNeon signal showing the result of EdU labelling after 16h incubation with EdU. **k.**
386 Histograms showing distribution of mNeon fluorescence by FACS of TINC reporter organoids
387 that were sorted according to Extended Data Fig. 7a into mNeon-high, -medium and -low cells
388 and allowed to reconstitute into heterogeneous organoids for 12 days. **l.** GSEA plots showing
389 enrichment of the TINC signature that was derived from single cell RNAseq and the 'RNF43-
390 mutation dependent secretory gene signature' as defined in Extended Data Fig.4b for TINC
391 reporter high versus low cells. **m.** Heatmap showing Z-scores for the expression of selected
392 genes (TINC markers, growth factors, WNT target genes and regenerative genes) in the TINC
393 reporter low, medium and high cells.

394

395

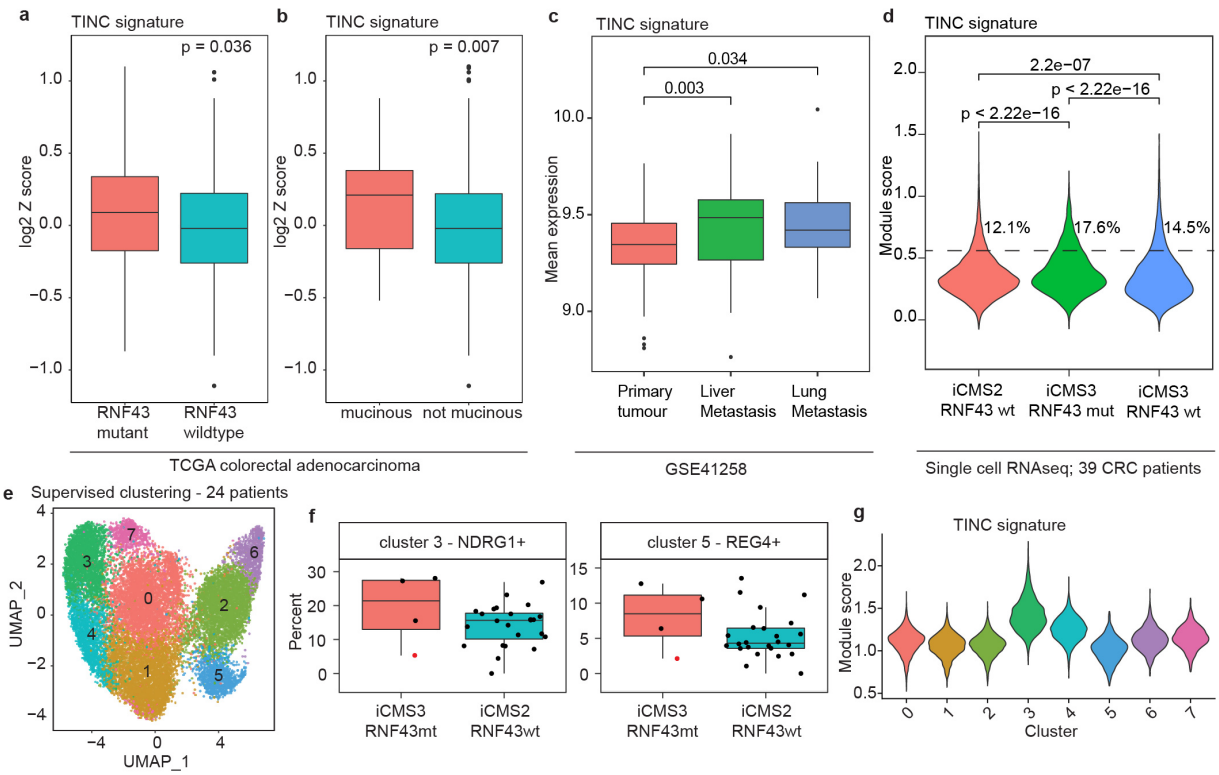

Fig. 4 | TINCs are enriched in *RNF43* mutant CRC patients and metastatic lesions. a, b. Box plots showing log2 Z-scores for the TINC signature (top 25 differentially expressed marker genes of HUB040 cluster 1 as determined in single cell RNAseq analysis) over the colon adenocarcinoma TCGA bulk RNA sequencing dataset grouped by *RNF43*-mutation status (n = 46 mut, 337 wt) (**a**) or pathology classification as mucinous (n = 37) or non-mucinous (n = 346) (**b**). **c.** Box plots showing expression of TINC signature (RMA normalization data) in microarray data of 186 primary tumours, 48 liver metastases and 20 lung metastases.[46] **d.** Violin plot showing single cell module scores for expression of genes from the TINC signature of single cells from 39 patients of Joanito et al[1] (iCMS2, 25 patients; iCMS3_RNF43wt, 10 patients; iCMS3_RNF43mut, 4 patients). Percentage of cells scoring above threshold of 0.55 is indicated. **e.** Reduced dimensionality (UMAP) visualisation of supervised clustering using 154 TINC signature genes of 18.320 single cells from 28 patients by Joanito et al[1]. **f.** Box plots showing the fraction of cells in cluster 3 or 5, divided by *RNF43* mutation status per patient.

410 The red dot marks a patient that has a *RNF43* and *APC* mutation. **g.** Violin plot showing single

411 cell module scores for expression of genes from the TINC signature grouped by cluster.

412

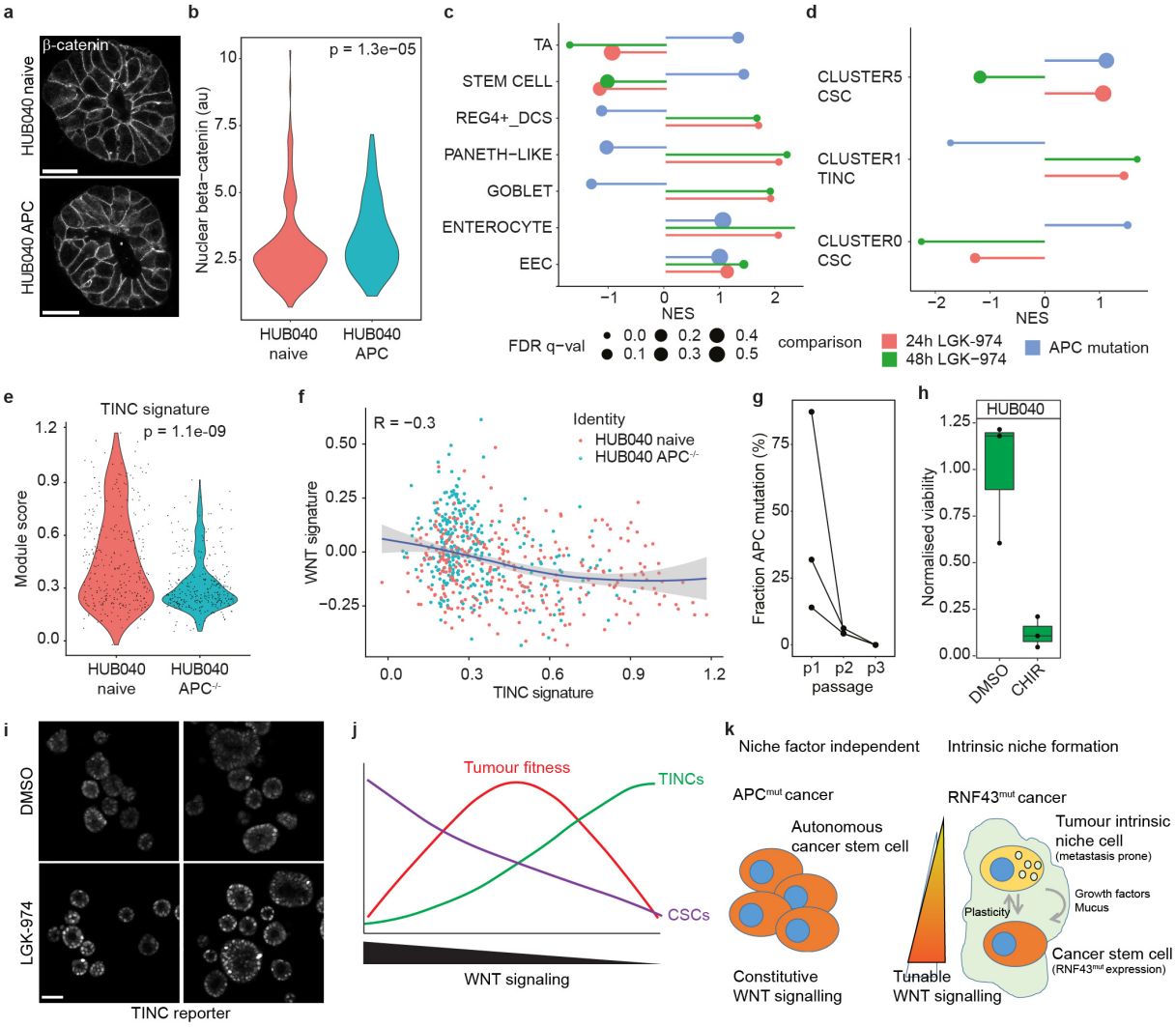

413

414 **Fig. 5 | A tight window of WNT signalling balances tumour niche cells and stem cells. a.**

415 Representative confocal microscopy pictures of organoids with IF labelling for β-catenin. Scale

416 bar = 20 µm. **b.** Violin plot showing quantification of nuclear β-catenin signal for 205-231 cells

417 per organoid line. **c, d.** Results of GSEA analysis comparing HUB040$^{APC\text{-}/\text{-}}$ with HUB040

418 (WNT activation, blue) and HUB040 treated with 100 nM LGK-974 for 24 or 48 hours with

419 DMSO treatment (WNT inhibition, orange and green) by gene signatures of colon-specific cell

420 types[13,14] (**c**) or HUB040-specific clusters as determined in Fig. 3a (**d**). x-axis shows the
421 normalized enrichment score (NES) and size of the dots shows the false discovery rate (FDR).
422 **e.** Violin plots showing single cell module scores for expression of genes from the HUB040
423 TINC signature grouped by organoid line of origin. **f.** Scatter plot showing inverse relation
424 between single cell module scores for expression of genes from the HUB040 TINC signature
425 and the Van der Flier WNT signature[47]. Colour of dots indicates line of origin. **g.** Line graph
426 showing fraction of *APC* mutant DNA after each passage in the competition assay of indicated
427 lines. n = 3. **h.** Box plots showing the relative viability of HUB040 organoids after 14 days
428 treatment with 5 μM CHIR99021 or DMSO control. n = 3 per condition. **i.** Representative
429 confocal microscopy images of HUB040 NDRG1-IRES-mNeon (TINC reporter) organoids
430 after three days treatment with LGK-974 or DMSO control. Scale bar = 50 μm. **j.** Schematic
431 representation of the optimal window of WNT-signalling for fitness of colorectal mucinous
432 adenocarcinomas. **k.** Diagram of the biological model presented in the discussion comparing
433 two routes towards of niche-independency in cancer.

434

435 **Extended Data Figures**

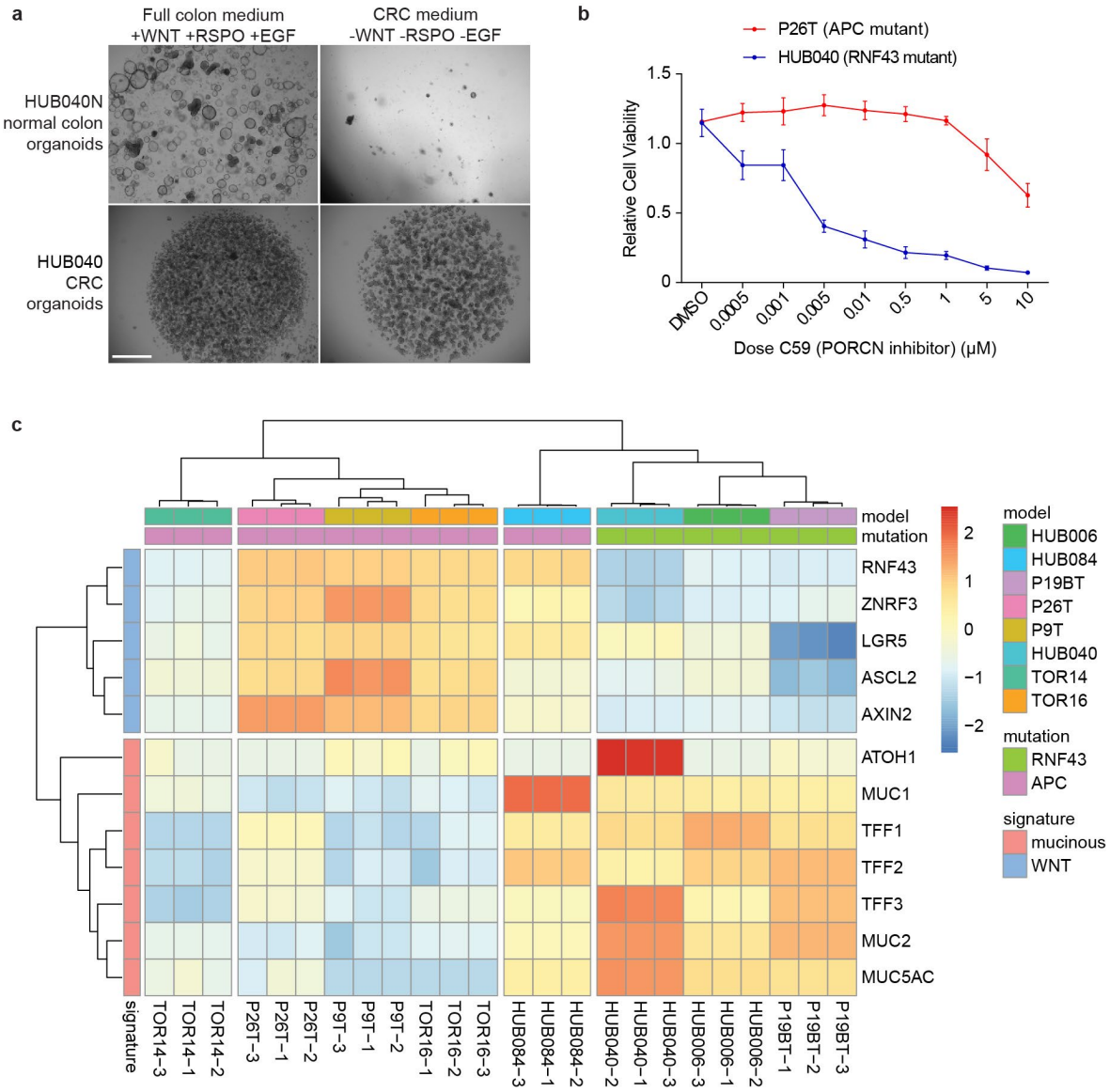

436

437 **Extended Data Fig. 1 | Patient-derived *RNF43* mutant CRC organoids are growth factor**
438 **self-sufficient. a.** Representative brightfield images showing healthy colon organoids and
439 HUB040 CRC organoids cultured in CRC culture medium or complete colon organoid medium
440 (including WNT, EGF and RSPO) for one passage and 14 days in total. Scale bar = 1000 μm.
441 **b.** Line graphs showing normalized viability of HUB040 and P26T organoids treated with
442 indicated concentration of PORCN inhibitor C59 for 7 days. Data were normalized to PBS-
443 treated organoids. n = 2, mean + sd **c.** Heatmap of gene expression data for WNT markers or

444 mucinous markers over a panel of CRC organoids (n = 8). Presence of *RNF43* or *APC* mutation
445 is indicated on top. Unsupervised clustering into four groups shows that *RNF43*-mutant
446 organoids cluster together in a low-WNT, high-mucinous group. Coloured bar represents row
447 z-scores of normalised counts

448

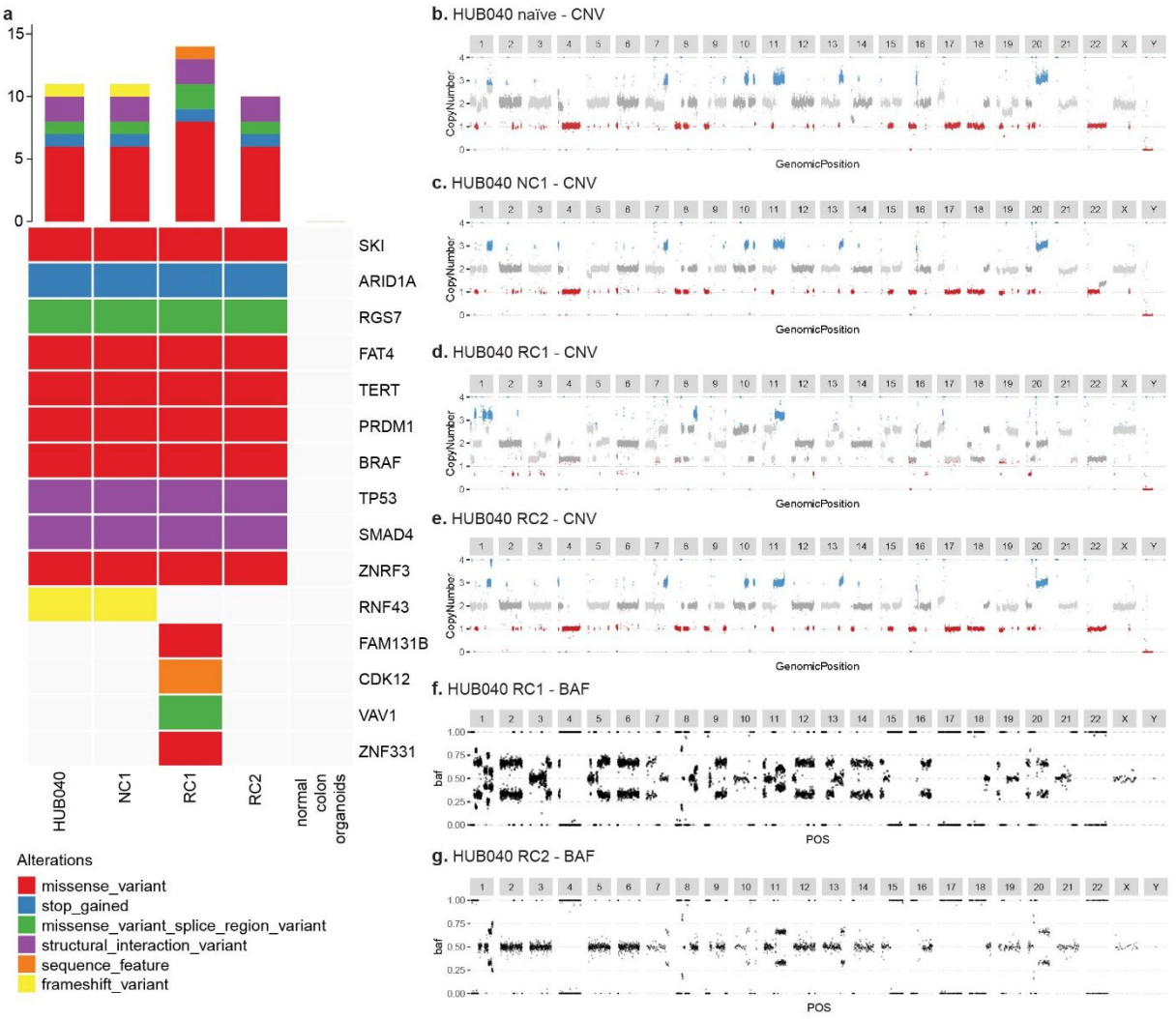

449

450 **Extended Data Fig. 2 | Whole genome sequencing analyses of HUB040 and clonal organoid**
451 **lines. a.** Oncoplot showing high-confidence putative driver mutations derived from whole
452 genome sequencing data of HUB040, normal colon organoids, NC1, RC1 and RC2. **b-e.** In
453 silico karyograms of HUB040 naïve CRC organoids (**b**), Non-corrected control HUB040 clone
454 (NC1) (**c**), *RNF43*-corrected clone 1 (RC1) (**d**) and *RNF43*-corrected clone 2 (RC2) (**e**). **f, g.**

455 B-allele frequency (BAF) plot for *RNF43*-corrected clone 1 (**f**) and RC2 (**g**) which is indicative

456 of a whole genome duplication event for RC1.

457

458

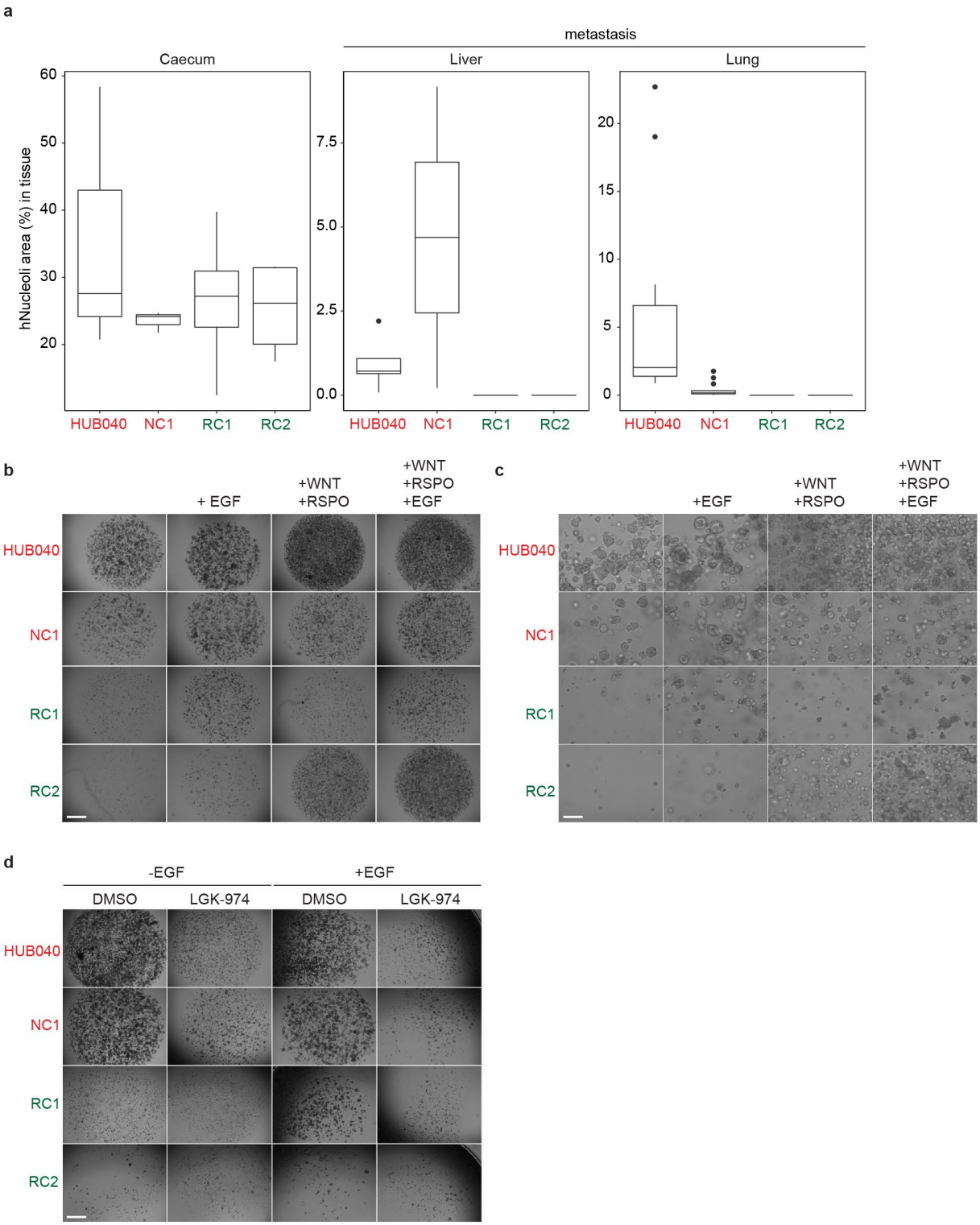

Extended Data Fig. 3 | Extended data belonging to Fig. 1. a. Box plots showing the fraction of tumour tissue relative to total tissue area for caecum, liver and lungs in mice that had a tumour or metastasis (see Fig. 1c for statistics). **b, c.** Representative low-magnification (2x, **b**) and high-magnification (10x, **c**) brightfield images of HUB040-derived clones cultured in CRC

464 medium supplemented with indicated growth factors for 14 days, passaged after 7 days. Scale
465 bar = 1000 µm (**b**) or 200 µm (**c**). **d.** Representative low-magnification brightfield images of
466 indicated HUB040 clones treated with 100 nM PORCN inhibitor LGK-974 or similar volume
467 of DMSO in CRC culture medium with or without EGF supplementation for 14 days, passaged
468 after 7 days. Scale bar = 1000 µm.

469

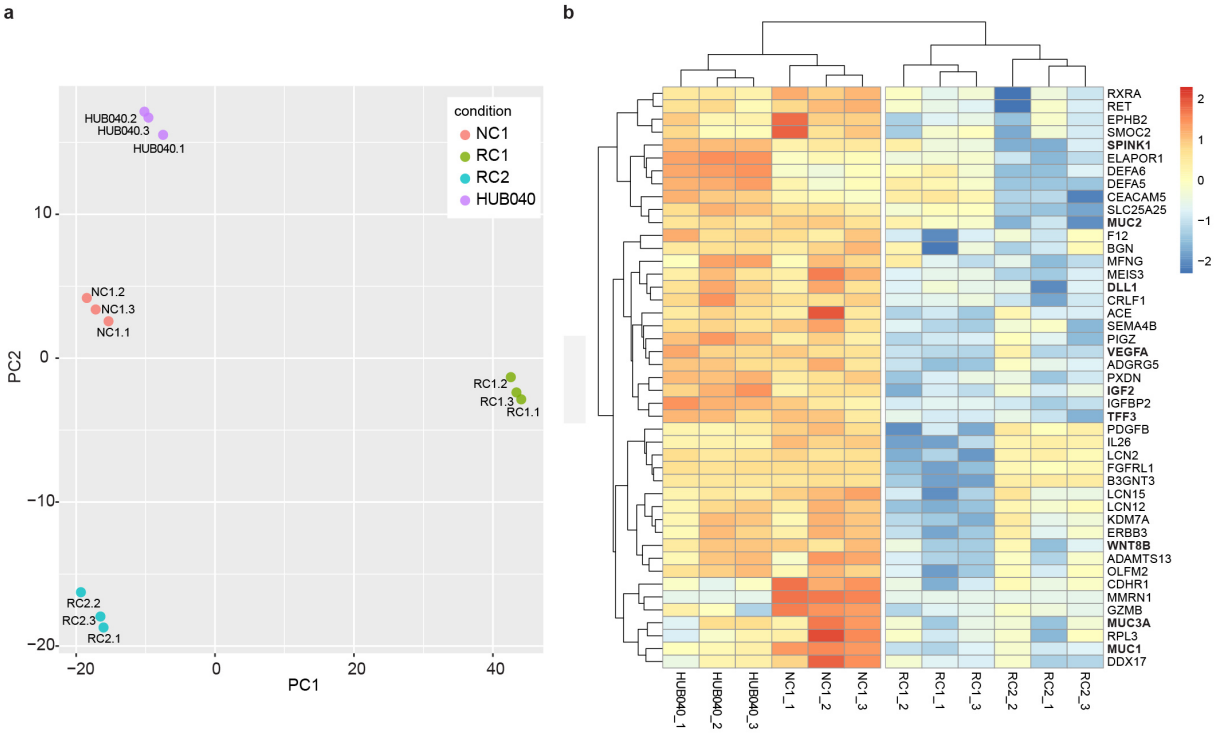

470

471 **Extended Data Fig. 4 | Extended data belonging to Fig 2. a.** Principle component analysis of
472 RNA sequencing data of HUB040 and *RNF43*-corrected and non-corrected clones. **b.** Heatmap
473 of downregulated secretory genes in *RNF43*-corrected HUB040 from a list of 3000+ genes
474 encoding for secreted proteins, as predicted by MDSEC.[48] Coloured bar represents row z-scores
475 of normalised gene counts.

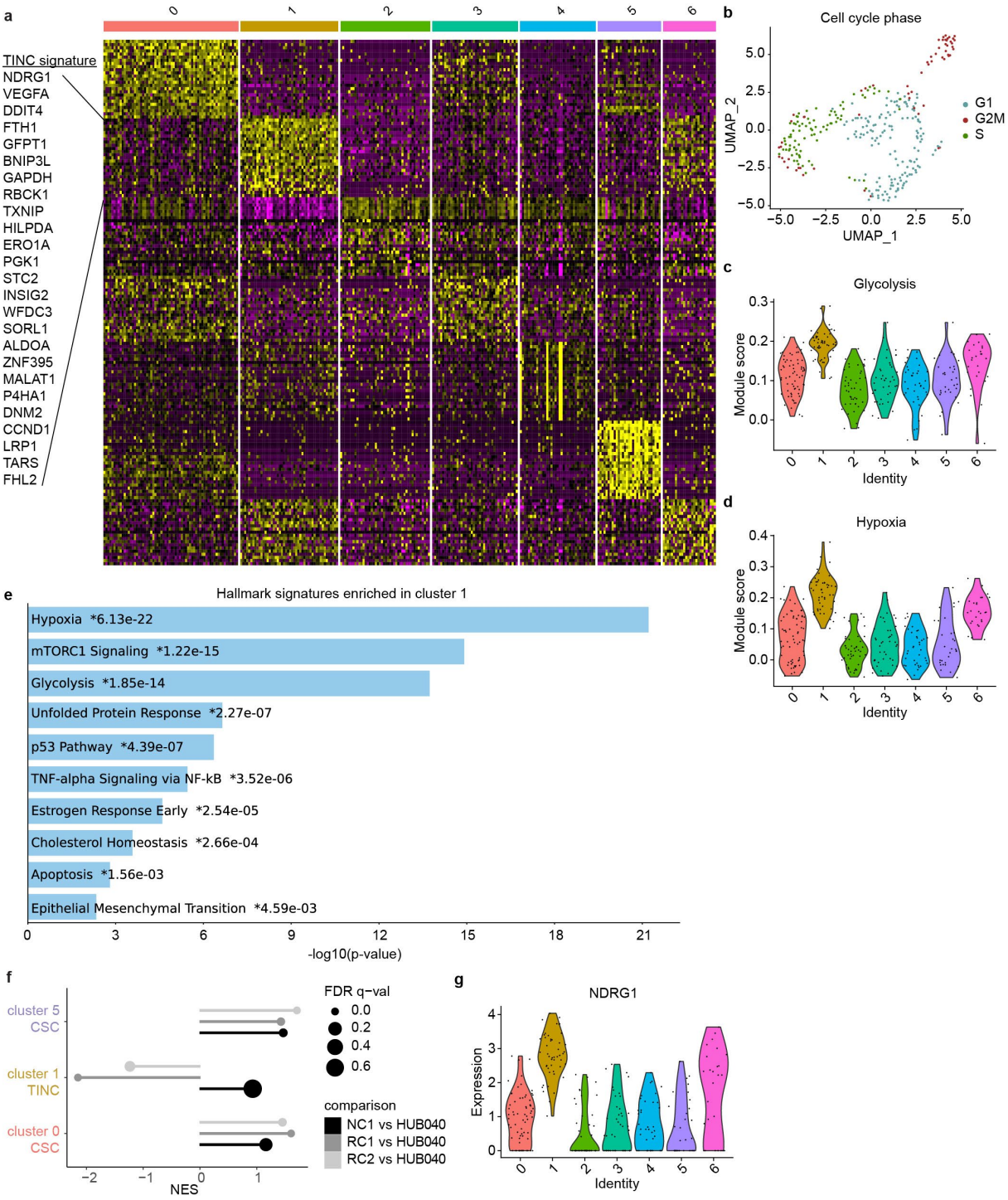

Extended Data Fig. 5 | Extended data single cell RNAseq HUB040. a. Single cell expression heatmap showing row Z-scores for top 25 marker genes for each cluster. Marker genes for cluster 1 are highlighted and later used as 'TINC signature'. **b.** Reduced dimensionality (UMAP) visualisation with cell cycle phase as determined by Seurat Analysis. **c, d.** Violin plots showing single cell module scores for expression of genes from the HALLMARK glycolysis

482 (**c**) and hypoxia (**d**) signatures[49] grouped by cluster. **e.** Bar plot showing p-value of the top ten
483 enriched HALLMARK gene signatures in the TINC marker genes list. **f. g.** Results of GSEA
484 comparing *RNF43*-corrected and non-corrected clones with HUB040 naïve by marker gene
485 signatures for three HUB040-specific clusters (CSC clusters 0 and 5 and TINC cluster 1). x-
486 axis shows the normalized enrichment score (NES) and size of the dots represents the false
487 discovery rate (FDR). **h.** Violin plots showing single cell expression levels for NDRG1.

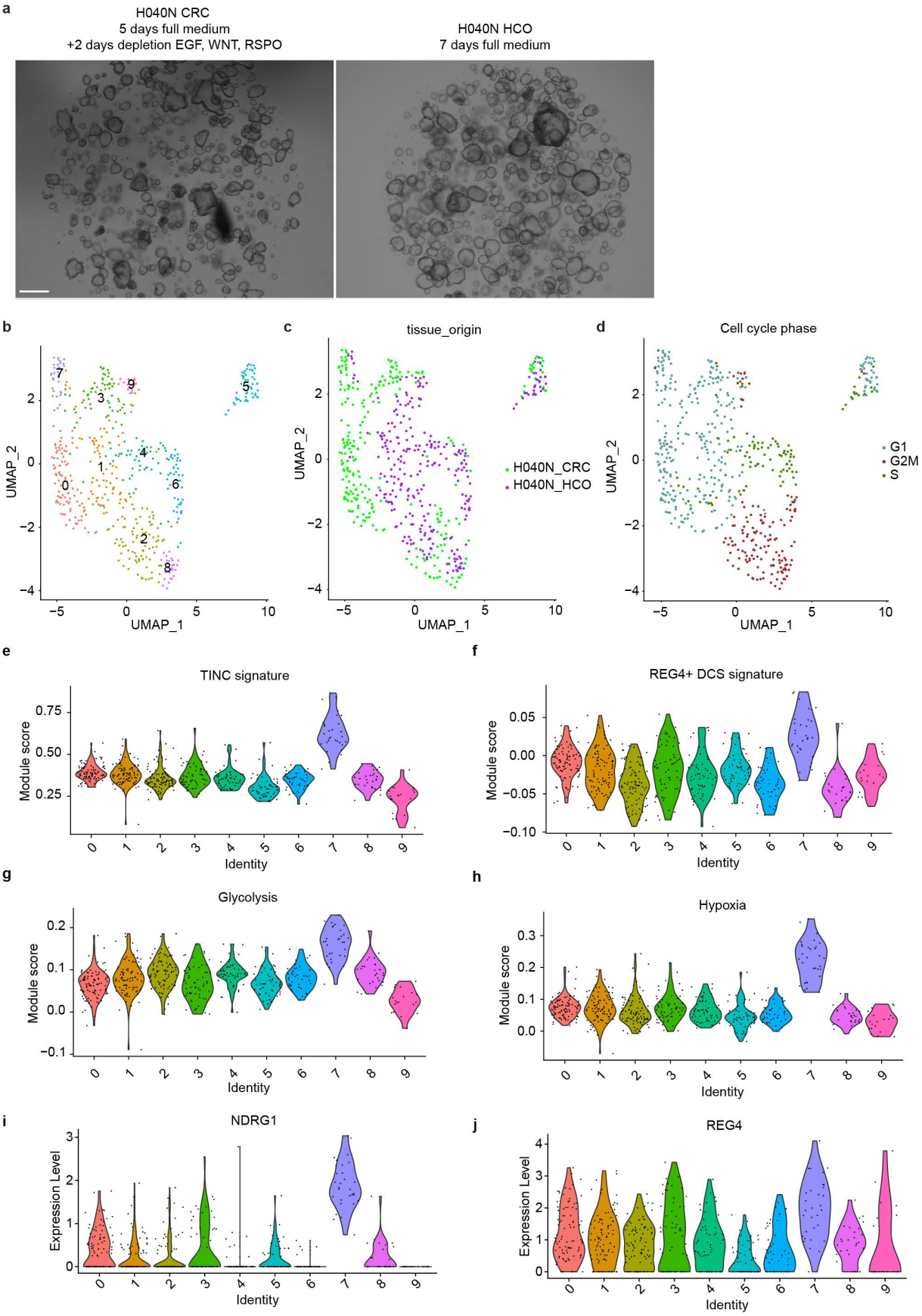
a
H040N CRC
5 days full medium
+2 days depletion EGF, WNT, RSPO
H040N HCO
7 days full medium
b
UMAP_2
UMAP_1
c
tissue_origin
H040N_CRC
H040N_HCO
d
Cell cycle phase
G1
G2M
S
e
TINC signature
Module score
Identity
f
REG4+ DCS signature
g
Glycolysis
h
Hypoxia
i
NDRG1
Expression Level
j
REG4

488

489 **Extended Data Fig. 6 | Single cell RNAseq normal colon organoids (HUB040N). a.**
490 Representative brightfield images of HUB040N normal colon organoid cultures in CRC
491 medium or full (HCO) medium that were used for single cell isolation and sequencing. Scale
492 bar = 1000 µm. **b.** Dimension reduction (UMAP) plot of single cell RNA sequencing data of
493 HUB040N organoids. Results of unsupervised clustering are colour-coded per cluster. **c, d.**
494 UMAP visualisation plotted for tissue of origin (**c**) or cell cycle phase (**d**) plotted. **e-h.** Violin
495 plots showing single cell module scores for expression of genes from the HUB040 TINC (**e**).
496 REG4+ deep crypt secretory cell (DCS)[13] (**f**). HALLMARK glycolysis[49] (**g**) or HALLMARK
497 hypoxia[49] (**h**) signature grouped by cluster. **i, j.** Violin plots showing single cell expression
498 levels for NDRG1 (**i**) and REG4 (**j**).

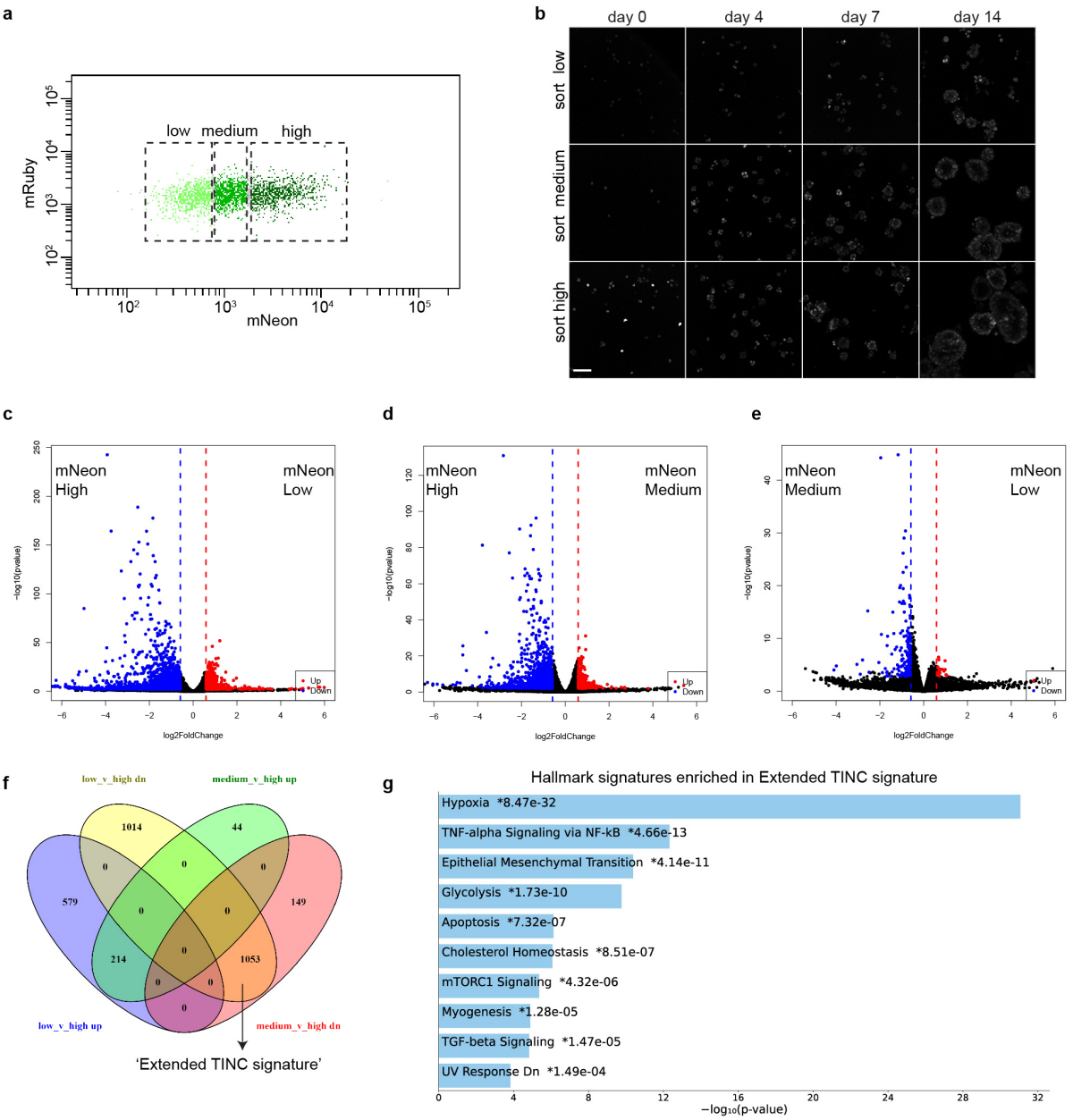

Extended Data Fig. 7 | Extended data TINC reporter. a. Histogram of mNeon signal for FACS sorted organoid: sorted populations are indicated. **b.** Representative confocal microscopy images of HUB040 NDRG1-IRES-mNeon (TINC reporter) organoids 0, 4, 7 and 14 days after plating of sorted cell populations. Scale bar = 50 µm. **c-e.** Volcano plots of differential gene expression of mNeon-low vs mNeon-high (**c**), mNeon-medium vs mNeon-high (**d**) and mNeon-low vs mNeon-medium (**e**) cells. Significantly (FC > 1.5 and $p < 0.05$) up and down regulated genes are plotted as red and blue dots respectively. **f.** Venn-diagram comparing differentially expressed genes as determined in **c** and **d** and defining and 'Extended TINC signature' as genes

508 upregulated in mNeon high cells compared to mNeon medium and mNeon low cells. **g.** Bar
509 plot showing p-value of the top ten enriched HALLMARK gene signatures in the Extended
510 TINC signature.

511

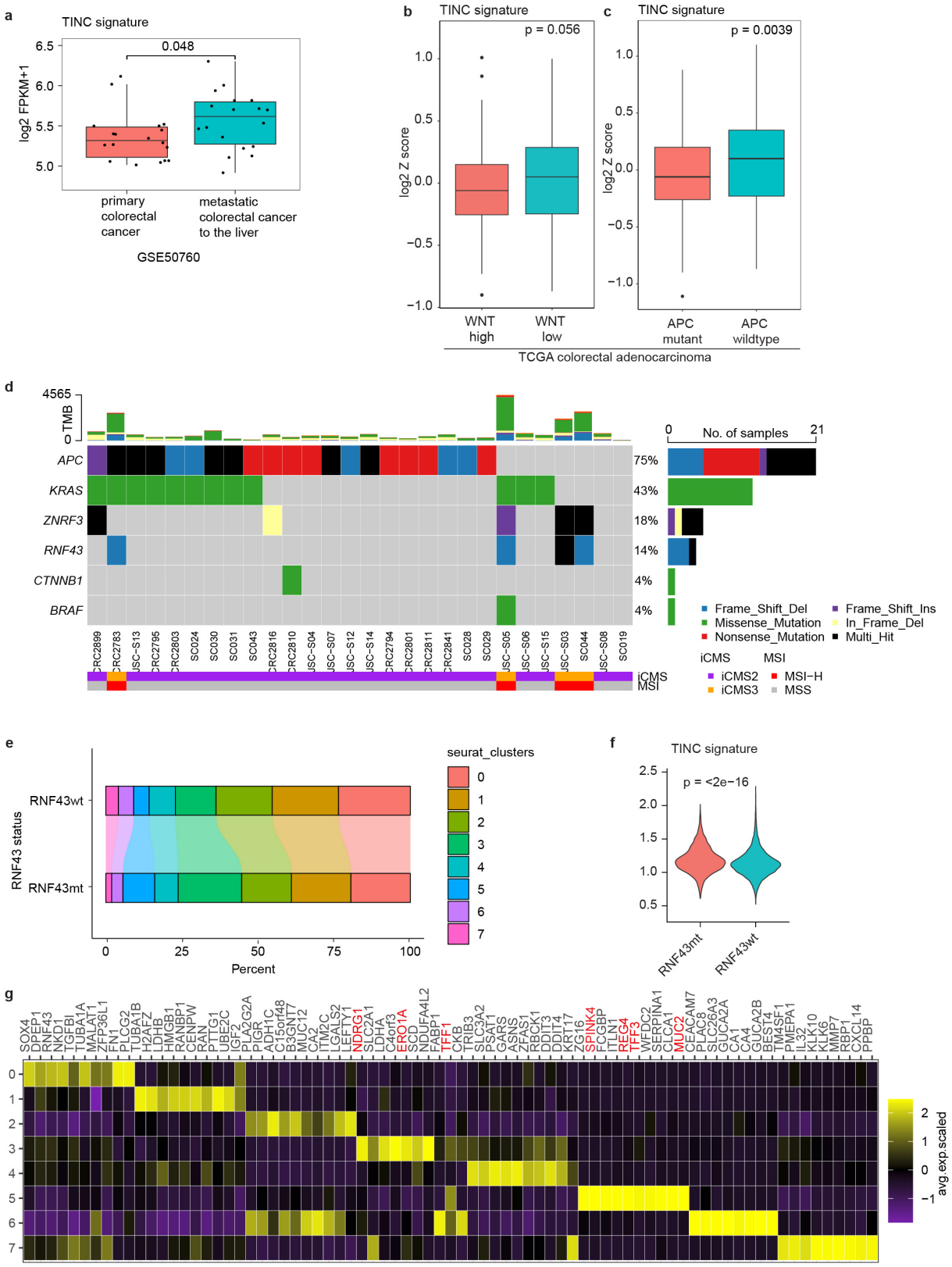

Extended Data Fig. 8 | Extended data belonging to Fig 4. a. Box plots showing expression of TINC signature (log2 FPKM +1) in RNA sequencing data of 18 paired primary colon tumours and liver metastases[50]. **b, c.** Box plots showing log2 Z-scores for the TINC signature

516 over the colon adenocarcinoma TCGA bulk RNA sequencing dataset grouped by WNT
517 signalling pathway activity as the upper and lower quartile of the Z-scores for the intestinal
518 WNT/TCF signature[47] (n = 95 each) (**b**) or *APC* mutation status (n = 277 mut, 106 wt) (**c**). **d.**
519 Oncoplot showing driver mutation status of the 28 patients included in single cell sequencing
520 cohort[1]. **e.** Alluvial plot comparing the fractions of cells per cluster for *RNF43* wildtype or
521 *RNF43* mutant patient groups. **f.** Violin plots showing single cell module scores for expression
522 of genes from the TINC signature grouped by *RNF43*-mutation status. **g.** Marker gene analysis
523 of the single cell patient data. Genes of interest are coloured red.

524

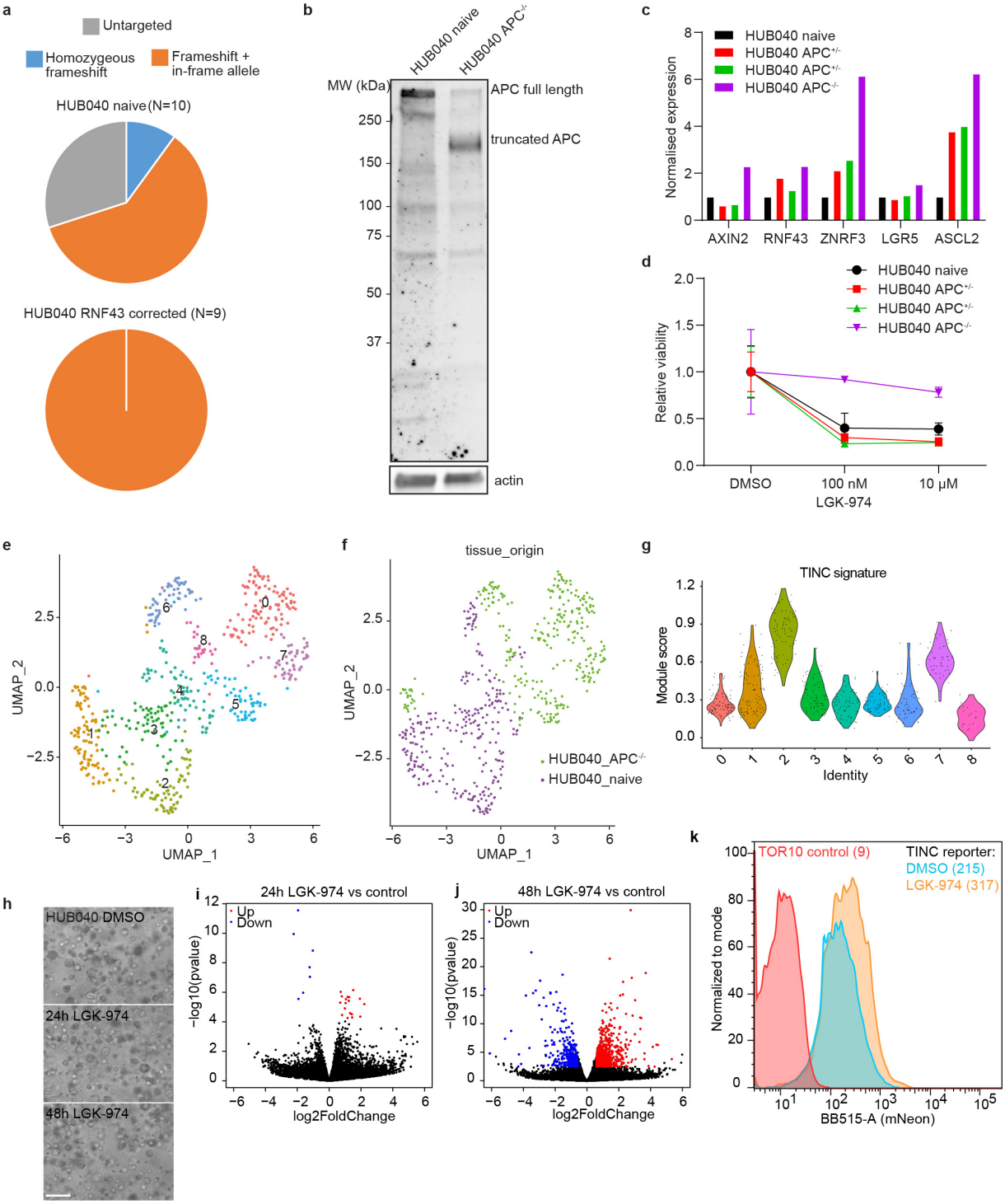

525

526 **Extended Data Fig. 9 | Extended data belonging to Fig 5. a.** Pie charts showing the various
527 genotypes found in *APC* targeted single clones of HUB040 and HUB040 RC2 organoids. **b.**
528 Western blot showing truncated APC protein expression in homozygous *APC* mutant HUB040.
529 **c.** Bar plot showing expression values, as measured by RT-qPCR, of classical WNT target genes
530 in HUB040 organoids with CRISPR induced heterozygous (two clones) or homozygous (one

531 clone) *APC* mutation normalized to naïve HUB040. **d.** Line graph showing relative viability of
532 naïve HUB040 organoids, or HUB040 with heterozygous or homozygous *APC* mutation after
533 seven days treatment with indicated concentration of PORCN-inhibitor LGK-974 or DMSO
534 control. Dots indicate mean and SD. n = 3. **e.** Dimension reduction (UMAP) plot of single cell
535 RNA sequencing data of naïve and *APC* mutant HUB040 organoids. Results of unsupervised
536 clustering are colour-coded per cluster. **f.** UMAP colour-coded per organoid line of origin. **g.**
537 Violin plots showing single cell module scores for expression of genes from the HUB040 TINC
538 signature grouped by cell cluster. **h.** Representative 10x brightfield images of organoid cultures
539 used for RNA isolation. Organoids were treated with 100 μM LGK-974 for 24 or 48 hours, or
540 with vehicle control (DMSO). Scale bar = 200 μm. **i, j.** Volcano plot of differential gene
541 expression between 24h (**i**) or 48h (**j**) LGK-974 treated HUB040 organoid versus DMSO treated
542 HUB040 organoids. Significantly (FC > 1.5 and $p < 0.05$) up and down regulated genes are
543 plotted as red and blue dots respectively. **k.** Histogram showing FACS analysis of HUB040
544 NDRG1-IRES-mNeon reporter organoids after three days treatment with LGK-974 or DMSO
545 control. Mean fluorescence intensity is indicated.

546 **Methods**

547 **Patient material**

548 The collection of colorectal tissue for the generation of healthy colon and CRC organoids was
549 performed according to the guidelines of the European Network of Research Ethics Committees
550 (EUREC) following European, national and local law. In all cases, patients signed informed
551 consent after ethical committees approved the study protocols. Organoids identified by HUB
552 codes *HUB-02-B2-040* (HUB040, CRC) and *HUB-02-A2-040* (HUB040N, normal colon) are
553 catalogued at https://huborganoids.nl/ and can be requested at info@huborganoids.nl.
554 Distribution to third (academic or commercial) parties will have to be authorized by the Biobank
555 Research Ethics Committee of the University Medical Center Utrecht (TCBio) at request of
556 Hubrecht Organoid Technology (HUB). P26T (CRC) was established in a previous study.[10]

557

558 **Organoid culture**

559 Healthy colon organoids and CRC organoids were cultured according to previous protocols[10].
560 In short, organoids were cultured in drops of Matrigel (Corning) or BME (R&D systems), and
561 the medium was refreshed every two or three days. CRC organoids were passaged using
562 TrypLE Express (Life Technologies) incubation at 37 °C. Healthy colon organoid were
563 passaged using mechanical shearing (pipetting). Healthy colon organoids were cultured in
564 advanced DMEM/F12 medium (Invitrogen), supplemented with 1% Penicillin/Streptomycin
565 (P/S, Lonza), 1% Hepes buffer (Invitrogen), 1% Glutamax (Invitrogen), 1x B27 (Invitrogen),
566 10 mM Nicotinamide (Sigma-Aldrich), 1.25 mM N-acetylcysteine (Sigma-Aldrich), 50 ng/mL
567 EGF (PeproTech), 500 nM TGF-b type I receptor inhibitor A83-01 (Tocris), 10 µM P38
568 inhibitor SB202190 (Sigma-Aldrich), 50% Wnt3a-CM (homemade) or 1% surrogate WNT-CM
569 (homemade)[51], 10% Noggin-CM (homemade), 20% Rspo1-CM (homemade) and 100 µg/mL

570 Primocin (Invitrogen) (full medium). Colorectal carcinoma organoids were cultured in medium
571 without EGF, WNT and RSPO (CRC medium), unless stated otherwise. *RNF43*-corrected
572 (RC), non-corrected (NC) HUB040 clones were maintained in full HCO medium to prevent
573 negative selection against growth factor dependence.

574

575 **CRISPR strategy and design**

576 To correct the *RNF43* P441fs mutation back to wildtype, HUB040 organoids were
577 electroporated with a single stranded HDR template (ss-oligo) and Cas9-gRNA. The ss-oligo
578 was designed according to previously established optimal rules.[52,53] Briefly, the *RNF43*
579 mutation in HUB040 is a five base pair duplication, which was corrected in the template. The
580 template was an asymmetric template oligo complementary to the non-target strand overlapping
581 the Cas9 cut site with 36 bp extension on the PAM-distal side, and with a 91-bp extension on
582 the PAM-proximal side of the break. The ss-oligo was ordered at Integrated DNA Technologies
583 with phosphorothioate modifications of the last two nucleotide bonds at the 3' and 5' end
584 (sequence:
585 TATGCACAAGGCTGGGGAATGAGCCACCTCCAATCCACCTCACAGCACCCTGCTG
586 CTTGCCCAGTGCCCCTACGCCGGGCCAGGCCTCCAGACAGCAGTGGATCTGGAGA
587 AAGCTATTGCACAGAACGC). A gRNA was chosen using the Benchling tool
588 (https://benchling.com) that created a double stranded break close to the mutation (sequence:
589 CCAGATCCACTGCTGTCAGG) and cloned in pSpCas9(BB)-2A-Puro (Addgene, 48139).

590 APC mutations were introduced by targeting the mutation cluster region (MCR) in the *APC*
591 gene using previously reported gRNA (sequence: TACATCTGCTAAACATGAG).[26]

592 Reporter targeting vector was generated by altering *HR180-LGR5-iCT* plasmid (Addgene
593 #129094) into a plasmid compatible with insertion of homology arms using golden-gate

594 cloning[54]. iCaspase-T2A-tdTomato sequence was removed and swapped for mNeonGreen-NLS
595 using a combination of Q5® High-Fidelity DNA Polymerase and the In-Fusion HD Cloning kit
596 (Takara). Final targeting vector was generated by insertion of homology arms (~600bp each)
597 flanking the targeted region downstream of NDRG1 to obtain the NDRG1-specific *IRES-*
598 *mNeonGreen-NLS-WPRE-bGHpA-EF1-Ruby-T2A-Puro-SV40pA* targeting plasmid. gRNAs
599 were cloned into pSpCas9(BB)-2A-Puro using golden gate cloning (sequence:
600 CCGGACTCTGATCTCTGTAG)).)).

601

602 **Electroporation**

603 Organoid electroporation was performed as previously described[55]. Briefly, organoids were
604 grown in antibiotic-free medium including 10 µM Y-27632 (Selleck chemicals) for two days
605 before electroporation. 24 hours before electroporation, 1.25% DMSO was added to the culture
606 medium. For electroporation, the NEPA21 electroporator was used with the configuration
607 reported by Fujii et al.[55]. For *RNF43* correction and generation of TINC-reporter, 5 µg of Cas9-
608 gRNA and 5 µg template were transfected. For other CRISPR targeting, 10 µg of Cas9-gRNA
609 was transfected. Organoids were recovered for two days by adding medium supplemented with
610 10 µM Y-27632. From five days post-electroporation organoids were grown in full medium.
611 For CRISPR-engineered organoids, single clones were established by manual picking of
612 individual organoids derived from single cells and genotyped. Reporter lines were selected by
613 puromycin treatment and sorted for the constitutive mRuby fluorophore and single cell derived
614 clones were picked manually and genotyped.

615

616 **Genotyping**

617 For genotyping of genome-edited organoids, genomic DNA was isolated using QIAamp DNA
618 micro kit (Qiagen). PCR amplification performed using using GoTaq Flexi DNA polymerase
619 (Promega) and products were loaded on an agarose gel. Gel fragments of expected sizes were
620 isolated using QIAquick gel extraction kit (Qiagen) and sequenced by Sanger sequencing.
621 Knockout and Knockin efficiencies were determined using the TIDE[56]
622 (http://shinyapps.datacurators.nl/tide/) and TIDER[57] (http://shinyapps.datacurators.nl/tider/)
623 tools respectively. Manual verification of genotypes for clonal lines was done in Benchling.

624 HUB040 NDRG1-IRES-mNeon clonal organoid lines were genotyped to confirm homozygous
625 integration of the knock-in construct using gel electrophoresis of PCR products.

626 Primers used for genotyping are listed in Supplementary Table 1.

627

628 **Whole-Genome Sequencing and mapping**

629 Genomic DNA of naïve HUB040 and clonal organoid lines was isolated using QIAamp DNA
630 micro kit (Qiagen) and DNA libraries for Illumina sequencing were generated by using standard
631 protocols (Illumina) Libraries were sequenced on a NovaSeq 6000 S4 platform with 2 x 150
632 bp read length to 30 times base coverage.

633 Sequencing reads were mapped against human reference genome GRCh38 by using Burrows-
634 Wheeler Aligner v0.7.17 mapping tool[58] with settings 'bwa mem -c 100 -M'. Sequence reads
635 were marked for duplicates by using Sambamba[59] v0.6.8 and sequence read quality scores were
636 recalibrated with GATK[60] BaseRecalibrator v2.7.2. CNVs detection was performed with
637 Control-FREEC[61] v11.56. Full pipeline description and settings are also available
638 at: https://github.com/UMCUGenetics/IAP.

639

640 **Mutation calling and filtering**

641 Mutation calling and filtering was performed on multi-sample vcfs generated by IAP using
642 HaplotypeCaller from GATK v.4.1.3.0. GATK's VariantFiltration was used for variant quality
643 evaluation with options: "--filter-expression 'QD < 2.0' --filter-expression 'MQ < 40.0' --filter-
644 expression 'FS > 60.0' --filter-expression 'HaplotypeScore > 13.0' --filter-expression
645 'MQRankSum < -12.5' --filter-expression 'ReadPosRankSum < -8.0' --filter-expression 'MQ0
646 >= 4 && ((MQ0 / (1.0 * DP)) > 0.1)' --filter-expression 'DP < 5' --filter-expression 'QUAL <
647 30' --filter-expression 'QUAL >= 30.0 && QUAL < 50.0' --filter-expression 'SOR > 4.0' --
648 filter-name 'SNP_LowQualityDepth' --filter-name 'SNP_MappingQuality' --filter-name
649 'SNP_StrandBias' --filter-name 'SNP_HaplotypeScoreHigh' --filter-name
650 'SNP_MQRankSumLow' --filter-name 'SNP_ReadPosRankSumLow' --filter-name
651 'SNP_HardToValidate' --filter-name 'SNP_LowCoverage' --filter-name 'SNP_VeryLowQual' -
652 -filter-name 'SNP_LowQual' --filter-name 'SNP_SOR' -cluster 3 -window 10".

653 Subsequently, SNPEffFilter[62], SNPSiftDbnsfp (database dbNSFP3.2a[63];, GATK
654 VariantAnnotator (database COSMIC v.89), and SNPSiftAnnotate (database GoNL release 5)
655 were used for variant annotation.

656 Finally, to obtain catalogues of high-quality somatic mutation calls, we applied post-processing
657 filtering steps, per sample, as described below (all scripts are available at:
658 https://github.com/ToolsVanBox/SMuRF).

659 Briefly, only variants were considered if present on autosomal chromosomes, passed
660 VariantFiltration with a GATK phred-scaled quality score ≥ 100, had a base coverage of at least
661 10X, had a mapping quality (MQ) score of 60, did no overlap with single nucleotide
662 polymorphisms (SNPs) in the Single Nucleotide Polymorphism Database v146 and a panel of
663 unmatched normal human MSC and fetal genomes (BED-file available upon request), had a

664 GATK genotype score (GQ) of 99 (indel/sbs in clonal sample, or indel in paired control) or
665 higher than 10 (sbs in paired control), had a variant allele frequency (VAF) of >=0.1 to exclude
666 *in vitro* accumulated mutations.

667

668 **Identification of driver mutations**

669 Single base substitutions or indels were considered as driver mutations when they have a MQ
670 of 30, a minimal base coverage of 10x, had a VAF equal or higher than 0.1, or present in driver
671 genes COSMIC cancer gene consensus (version of 9/5/2019), were also annotated as missense,
672 frameshift, stop-gain, insertion or deletion, had either a high or moderate expected effect as
673 annotated by SnpEff, and were not present in the Single Nucleotide Polymorphism Database
674 v146 and a panel of unmatched normal human MSC and fetal genomes (BED-file available
675 upon request). Oncoplot (Extended Data Fig. 2a) was generated with the ComplexHeatmap[64]
676 v2.12.0 package from Bioconductor.

677 Structural variant and chromosomal copy-number alteration calling was performed using the
678 GRIDSS-purple-linx[65] pipeline developed at the Hartwig Medical Foundation.

679

680 ***In vivo* subcutaneous tumorigenesis**

681 Animal experiments were approved by the Competent Authority, The Netherlands (License
682 number AVD115002016614), which is advised by the Animal Ethics Committee. Animal work
683 protocol (614-1-22) was approved by the Animal Welfare Body and were performed in
684 accordance with the Dutch Law on Animal Experiments and the European Directive
685 2010/63/EU. Healthy 8–10 week old 25–30 g male *NOD.Cg-Prkdc*^{scid} *Il2rg*^{tm1Wjl}*/SzJ* (NSG)
686 mice were supplied by Charles River. Animals were randomly allocated in groups of three mice

687 into individually ventilated cages. Animals were kept at room temperature under 12 hours
688 light/dark cycles and received standard chow pellets and water ad libitum. HUB040 organoids
689 were dissociated five days after passaging into single-cells by TrypLE Express incubation for
690 5 min at 37 °C. A cell-matrigel (1:1) suspension was prepared with 5×10^6 cells/mL. Using a
691 1 mL syringe and 25G 0.5 × 16 mm needles, 100 µl of the suspension were subcutaneously
692 injected into the right flank of animals. Animal welfare was monitored by physical appearance,
693 behaviour, and body weight. Animals were sacrificed when the tumour volume (V) reached 1.5
694 mm^3, as measured by $V = 1/2 \times (\text{smaller diameter}^2 \times \text{larger diameter})$. Tumour tissue was
695 harvested for further immunohistochemical analyses. Sample sizes are outlined in the figure
696 legends. Mice were randomly assigned to experimental groups. No blinding method was used
697 for injection. No animals were excluded from downstream analysis.

698

699 **Orthotopic implantation in the caecum of NSG mice**

700 In order to evaluate the tumourigenic capacity of the organoids, murine orthotopic caecum-
701 implantation model[12] was used as described in animal work protocol (614-1-22). In summary,
702 day before implantation, HUB040 organoids were dissociated into single cells and 2.5×10^5
703 cells were plated in 10 µL drops of neutralized Rat Tail High Concentrated Type I Collagen
704 (Corning, C3867). Cultures were allowed to recover overnight at 37 °C, 5% (vol/vol) CO2.
705 NSG mice were treated with a s.c. dose of Carprofen (5 mg/kg, Rimadyl™) 30 min before
706 surgery and were subsequently sedated by using isoflurane inhalation anesthesia [~2%
707 (vol/vol) isoflurane/O2 mixture]. The caecum was exteriorized through a midline abdominal
708 incision and a single collagen drop containing organoids was surgically transplanted in the cecal
709 submucosa. Carprofen was administrated s.c. post 24 hour surgery. Animal welfare was
710 monitored by physical appearance, behaviour, and body weight. Power analyses were carried

711 out prior to experiments being carried out to determine the minimum number of animals
712 required for each experiment. These analyses were informed by previous and / or preliminary
713 experiments. Animals were house vested in groups of four. Every group (i.e. cage) contained
714 mixture of mice transplanted with both organoid genotypes. No animals were excluded from
715 downstream analysis. The biotechnician was blinded to the group allocation of the animals
716 during the experiment.

717

718 **Immunohistochemistry (IHC)**

719 Mouse tissues with or without organoid-initiated tumours/metastases were fixed in 4%
720 formaldehyde solution and paraffin embedded. Sections of 4 µm thickness were made. Prior to
721 the staining, tissue sections were deparaffinized and rehydrated. Endogenous peroxidase
722 activity was blocked with 1.5% hydrogen peroxide for 30 min. Heat-induced antigen retrieval
723 was carried out using citrate buffer pH6.0 for 20 min, followed by the cooling of tissue sections
724 for 20 min. Sections were incubated overnight at 4 °C with primary antibodies (anti-hNucleoli
725 clone NM95, Abcam (ab190710) 1:1000 and anti-Mucin2 clone (H-300), Santa Cruz (sc-
726 15334), 1:100) diluted in PBS with 0.1% Sodium azide and 3% BSA. The next day, sections
727 were washed three times with 0.05% Tween-PBS solution for 5 min, followed by a 1 hour
728 incubation with the HRP-conjugated secondary antibody. Subsequently, sections were washed
729 three times with 1× PBS for 5 min and developed with 3,3'-Diaminobenzidine (DAB)
730 chromogen for 10 min at room temperature in the dark. Sections were rinsed under running tap
731 water for 10 min and counterstained with hematoxylin, followed by dehydration and mounting.

732 Stainings were scanned using NanoZoomerXR whole slide scanner (Hamamatsu) at
733 40X magnification, with a resolution of 0.25 µm/pixel. Quantification of the scans was
734 performed using QuPath program analysis program[66]. Target of interest (tumour or distinct

735 immune populations) was quantified using QuPath's Trained Pixel classification command that
736 allows an automated recognition of background, tissue (hematoxylin) and DAB staining areas.
737 The percentage of target of interest area was then calculated by using the following formula:
738 DAB area / (DAB + tissue– background area) * 100.

739

740 **Reconstitution assays using growth factor and drug treatments**

741 Single cells from organoid were harvested using TrypLE incubation at 37 °C. Cells were filtered
742 through a 40 µm nylon cell strainer (Falcon). Cells were counted and seeded in a $1*10^6$ cells /
743 mL dilution in Matrigel/BME. Cultures were incubated in standard culture medium with
744 indicated additions/depletions of factors and drugs, which was replenished every 2-3 days. After
745 seven days, brightfield images were taken using an EVOS imaging system and organoids were
746 split 1:2 similar as mentioned before, after which outgrowth was monitored again for seven
747 days. Quantitative viability assays were performed by CellTiter-Glo® (Promega) or Alamar
748 Blue® (Thermo Fisher) according to manufacturer instructions. Pictures are shown for a
749 representative experiment, which was performed at least three times. Normalized viability data
750 was combined from multiple experiments and two or three technical replicates per experiment.

751

752 **Bulk RNA sequencing**

753 Organoids were lysed in RLT lysis buffer (Qiagen) + 1% β-mercapto-ethanol; seven days after
754 passaging. Biological triplicates were employed that were passaged and lysed at separate
755 moments. For the LGK-974 experiments, organoids were treated with 100 nM LGK-974 or a
756 DMSO volume control for 24 or 48 hours prior to lysis. RNA was obtained using the Qiagen
757 QiaSymphony SP (Qiagen) according to the manufacturer's protocol. Library prep was
758 performed using Truseq RNA stranded polyA (Illumina). Libraries were sequenced on an

759 Illumina NextSeq2000 platform with 1x50bp reads. Single-end RNASeq reads were processed
760 using the UMCU RNASeq pipeline (v2.3.0) with default settings. Read quality was assessed
761 by FastQC (0.11.4) followed by splice-aware alignment against the human reference genome
762 (GRCh38) with STAR[67] (2.4.2a). RNA expression quantification was performed with htseq-
763 count (0.6.0) in reverse-stranded mode. Differential gene expression analysis was performed
764 with the DESeq2[68] (1.22.2) R package. In each comparison, genes were selected with an
765 absolute fold-change > 1.5 and p adjusted < 0.05. Generation of heatmaps and scatterplots was
766 done in using the pHeatmap and ggplot2 R packages.

767

768 **GSEA and gene signatures**

769 Gene set enrichment analyses (GSEA) were performed using the Broad Institute GSEA tool
770 (software.broadinstitute.org/gsea/index.jsp) with default settings, including permutation by
771 gene sets. HALLMARK genesets were derived from the Molecular Signatures Database.[49]
772 Geneset for REG4$^+$ deep crypt secretory cells (DCSs) was defined as human orthologues
773 (identified by bioDBnet) of the >2 fold upregulated genes with a p-value < 0.05 in Reg$^+$ cells
774 compared to Lgr5$^+$ cells that were previously reported.[13] Gene sets for human colon specific
775 cell types were derived from a published single-cell transcriptome study (Wang et al. table
776 S2).[14] Genesets for HUB040 single cell clusters were defined by marker gene analysis using
777 the 'FindAllMarkers' command in Seurat comparing one cluster to all other clusters using a
778 wilcox test. Threshold for adjusted p-value was set at p < 0.05. The WNT signature was reported
779 previously by Van der Flier *et al.*[47]

780 For the analysis of secretory genes, a list of secreted proteins was downloaded from human
781 protein atlas ("Secreted proteins predicted by MDSEC")[48]. Downregulated secretory genes

782 were defined as: significantly downregulated in at least three comparisons and not upregulated
783 in the other comparison (RC1 vs HUB040, RC2 vs HUB040, RC1 vs NC1, RC2 vs NC1)

784

785 **Single cell RNA sequencing and analysis**

786 Single cells from organoid were harvested using TrypLE incubation at 37 °C, seven days after
787 passaging. Cells were filtered through a 40 µm nylon cell strainer (Falcon). scRNA-seq was
788 performed according to the Sort-seq protocol[69]. Libraries were sequenced on an Illumina
789 NextSeq500 at paired-end 60- and 26-bp read length and 75,000 reads per cell.

790 Reads were mapped to the hg38 reference genome. Analysis was performed with the R-package
791 Seurat[70] (4.0.4). Cells with 400-50000 unique features and 1000-7000 total transcript counts
792 were included in the analysis. Scores for gene signature expression were calculated using the
793 AddModuleScore function.

794 Signature enrichment in marker gene lists was determined using the Enrichr tool[71]
795 (https://maayanlab.cloud/Enrichr/).

796 To analyse fraction of TINCs in *RNF43*-corrected and non-corrected clones, cells were filtered
797 according to previously mentioned settings and for each cell a module score for the original
798 TINC signature was calculated. Cells with a module score > 0.61 were scored as TINC, which
799 corresponded to 16% of cells in the HUB040 naïve sample (which was the fraction of cells
800 mapping to cluster 1 in the original analysis). Data was plotted using ggplot2.

801 To validate the TINC signature in a human cohort, published RNAseq data of tumour epithelial
802 cells of colorectal cancer patients were used[1]. Twenty *RNF43* wildtype patients from iCMS2
803 cohort based on single-cell RNA sequencing and inferred CNV result and four *RNF43* mutant
804 patients were selected. After selecting patients, supervised clustering using 154 TINC signature

805 genes was performed with batch correction using harmony algorithm[72] to remove patient
806 specificity. Differential gene expression analysis was performed using the 'FindAllMarkers'
807 command in Seurat with logistic regression framework.

808

809 **TCGA data analysis**

810 Signature scores for indicated gene sets were calculated for each samples as log2 Z-score over
811 the total TCGA Colon Adenocarcinoma set (rpkm values of 382 samples - cbcoad) using the
812 R2 genomic analysis platform (http://r2.amc.nl). TINC signature was determined as the top 25
813 marker genes for cluster 1 in HUB040 (from Seurat marker gene analysis). *RNF43* mutation
814 status was determined by combining the list of *RNF43* mutant TCGA samples (derived from
815 C-bioportal) combined with results of re-analysis by Gianakkis *et al.*[27] calling additional
816 mutations that were falsely labelled as polymerase slipping errors in the original TCGA
817 analysis.[27] CMS classifications were derived from the Colorectal Cancer Subtyping Consortium
818 (CRCSC)[73], samples without CMS label have been left out of the analysis. Classification as
819 mucinous was derived from Cancer Type in cbioportal (mucinous adenocarcinoma of colon and
820 rectum). "High and low WNT" was defined as the upper and lower quartile of the Z-scores for
821 the intestinal WNT/TCF signature as reported by Van der Flier *et al.*[47].

822

823 **Immunofluorescence**

824 For staining of Mucin2, organoids were seeded in 15-well IBIDI angiogenesis chambers during
825 passaging and fixed 7-12 days later in 4% paraformaldehyde (PFA) (Sigma-Aldrich) for 60 min
826 at room temperature. The fixation was quenched using 0.05 M NH_4Cl and cells were
827 permeabilised with PBD0.2T (48,5mL PBS, 1mL 10%Triton, 0,5mL DMSO and 0,5g BSA)
828 for 20 min at room temperature. The organoids were incubated with primary antibodies diluted

829 in PBD0.2T at 4 °C overnight. Washes were performed with PBD0.2T after which secondary
830 antibodies were incubated for 3h at room temperature. Stained organoids were mounted using
831 IBIDI mounting medium.

832 For other stainings, organoids were cultured as usual. 7-12 days after passaging, matrix was
833 removed using dispase (Invitrogen) and organoids were transferred to 8-well IBIDI imaging
834 slide. Fixation, permeabilisation and antibody staining were performed inside the imaging slide,
835 as indicated above, except for primary antibody incubations were performed for one hour at
836 room temperature. Stained organoids were mounted using IBIDI mounting medium.

837 The following antibodies and dyes have been used for immunofluorescence: Mouse-anti-
838 Mucin2 (sc-515032, Santa Cruz, 1:200), Mouse-anti-β-catenin (610154, BD Transduction
839 Laboratories, 1:200), Rabbit-anti-KI67 (ab15580, Abcam, 1:200), Goat-anti-Mouse-Alexa-488
840 (A11029, Invitrogen, 1:600) Goat-anti-Rabbit-Alexa-647 (A21245, Invitrogen, 1:600),
841 Phalloidin-Alexa-647 (8940S, CST, 1:200) and Dapi (D9542, Sigma, 1:1.000). Images were
842 acquired with a Zeiss LSM700 confocal microscope.

843 Image processing was performed using FIJI (2.3.0). Nuclear β-catenin and TINC-reporter
844 intensity were quantified using the StarDist plugin (0.8.3)[74] with the Dapi staining used for
845 single nucleus segmentation. Data was analysed and plotted in R.

846

847 **Hybrid organoid co-culture, time-lapse imaging and analysis**

848 The protocol on generating hybrid organoid co-cultures has been described previously[15]. In
849 short: HUB040 naïve organoids were transduced with mCherry tagged H2B constructs and
850 HUB040 RC2 organoids with mNeon green tagged H2B constructs and selected by FACS
851 sorting. Six days post splitting, both lines were starved in CRC medium for 24 hours and at day
852 7 broken up into small clumps of cells that were mixed in 1:1 ratio. Cells were concentrated by

853 centrifugation, resuspended in a small volume of CRC medium and incubated at 37 °C for 30
854 min Cell aggregates were plated in 10 µL BME droplets in an 18 Well µ-Slide (IBIDI #81811).
855 Three days after plating, time-lapse microscopy was performed on an inverted LSM880 Fast
856 AiryScan scanning confocal microscope (Zeiss) using LSM scanning mode with a 488nm
857 Argon-laser and 561nm Diode-laser, equipped with a 20X dry immersion objective (Objective
858 Plan-Apochromat 20x/0.8 M27, Zeiss). Cells were kept in CRC medium at 37°C under 5% CO2
859 for the full duration of the experiment. Images were acquired with a Z-interval of 5µm covering
860 the full volume of the organoid and time-interval of one hour for a total duration on 60 hours.
861 Time-lapse images were processed and analysed following a previously described pipeline in
862 which depth-encoded movies were generated in which cell divisions and cell dead events were
863 scored[75]. The cell death / mitosis ratio was calculated as a proxy for organoid survival. Cell
864 numbers at the start of time-lapse were counted using Imaris software (Andor version 9.9.1).
865 Videos and snapshots of 3D-reconstructed representative organoids were made in Imaris.

866

867 **Flow cytometry analysis and sorting of organoids**

868 Single cells from organoid were harvested using TrypLE incubation at 37 °C. Cells were filtered
869 through a 40 µm nylon cell strainer (Falcon) and live-cells were measured at a FACS Celesta
870 with FACS Diva software (BD). The following fluorescent channels were used: BB515 for
871 mNeon, PE-CF594 for mRuby and PE-Cy5 for Alexa-647 labelled Edu.

872 EdU incorporation assays were performed by culturing organoids in CRC medium containing
873 10 µM EdU for 16 hours to cells, after which single cells were harvested, fixed in 4% PFA and
874 EdU-labeling was performed according to manufacturer instructions (Click-iT EdU Cell
875 Proliferation Kit for Imaging, Thermo Fisher).

876 Sorting of TINC-reporter populations was performed using a FACS Aria III machine (BD)
877 Populations were gated for viable single cells which were divided in three equal populations of
878 20-30% of the total based on mNeon histogram (example in Extended Data Fig 7a). Sorted cells
879 were directly lysed in RLT lysis buffer (Qiagen) for RNAseq analysis, or taken in culture for
880 organoid reconstitution, by seeding in a $1x10^6$ cells / mL dilution in BME.

881 Gated single cells were analysed in FlowJo (version 10.6.1).

882

883 **Western blot**

884 Organoids were collected in Cell Recovery Solution (Corning), incubated for 20 min on ice and
885 subsequently lysed in RIPA buffer containing protease and phosphatase inhibitors. Lysates
886 were boiled in 1x SDS sample buffer and ran on a pre-casted SDS-page gel (Mini protean, BIO-
887 RAD). Gels were transferred to a Immobilon-FL PVDF membranes (Millipore), which was
888 blocked for 1 hour at room temperature in 1:1 ratio Odyssey blocking buffer (LI-COR): PBS,
889 and stained against APC (sc-7930, Santa Cruz, 1:1.000) and Actin (691001, MP, 1:10.000)
890 overnight at 4 °C. Blots were stained with secondary antibodies IRDye-680 goat anti-rabbit
891 (926-32221, LI-COR, 1:10.000) and IRDye-800 goat anti-mouse (925-68070, LI-COR,
892 1:10.000) for 1 hour at room temperature in the dark. The Typhoon (GE Healthcare) infrared
893 imaging system was used for immunoblot analysis.

894

895 **RT-qPCR**

896 Organoids, seven days after passaging, or FACS-sorted cell populations were lysed in RLT
897 lysis buffer (Qiagen) + 1% β-mercapto-ethanol and RNA was purified using the RNeasy kit
898 (Qiagen) according to manufacturer's protocol. RNA was used as a template for cDNA

899 production using the iScript™ cDNA Synthesis Kit (Biorad) according to the manufacturer's
900 protocol. The synthesized cDNA was subsequently used in a qRT–PCR using IQ SYBR green
901 mix (Biorad) according to the manufacturer's protocol. Used primers are listed in
902 Supplementary Table 2

903 Expression of WNT target genes was corrected against house-keeping gene *GAPDH* and
904 normalized to the control.

905

906 **APC competition assay**

907 HUB040 and HUB040$^{APC-/-}$ organoids were split into single cells, counted and seeded in a 1:1
908 ratio. Mixed organoid populations were passaged once a week, and during each passage,
909 genomic DNA was harvested for genotyping the fraction of *APC* mutant alleles as indicated
910 above.

911

912 **Statistical analyses**

913 For RNA sequencing analysis, statistical significance was determined using the DESeq function
914 in R, which uses a Wald test (two-tailed), see detailed methods. Gene set enrichment was
915 performed as described in the methods. For other data, p values were calculated using the
916 'stat_compare_means' function of the ggpubr package (0.40.0) in R. For comparing two or
917 more groups of non-parametric data, a two-sample Wilcoxon test or Kruskal-Wallis were used
918 respectively.

919

920 **Data availability**

921 The scRNA-seq and bulk RNA-seq data generated in this study are available from Gene
922 Expression Omnibus (GEO) under the accession codes GSE213079 (scRNAseq), GSE213077
923 (bulk RNAseq various organoid lines), GSE212959 (bulk RNAseq RNF43-corrected and non-
924 corrected HUB040 organoids), GSE220128 (bulk RNAseq TINC reporter cells), GSE213068
925 (bulk RNAseq APC mutant and wildtype HUB040 organoids) and GSE213072 (bulk RNAseq
926 HUB040 organoids treated with LGK-974).

927 Published scRNA-seq data referenced in the study is available from Synapse under the
928 accession code syn26844071. Published microarray and bulk RNA-seq are available from Gene
929 Expression Omnibus (GEO) under the accession codes GSE41258 and GSE50760,
930 respectively.

931

932

933 **Methods references**

934 46. Sheffer, M. *et al.* Association of survival and disease progression with chromosomal
935 instability: A genomic exploration of colorectal cancer. *Proc. Natl. Acad. Sci. U. S. A.*
936 **106**, 7131–7136 (2009).

937 47. Van der Flier, L. G. *et al.* The Intestinal Wnt/TCF Signature. *Gastroenterology* **132**,
938 628–632 (2007).

939 48. Uhlén, M. *et al.* Tissue-based map of the human proteome. *Science (80-.).* **347**, (2015).

940 49. Liberzon, A. *et al.* The Molecular Signatures Database Hallmark Gene Set Collection.
941 *Cell Syst.* **1**, 417–425 (2015).

942 50. Kim, S. K. *et al.* A nineteen gene-based risk score classifier predicts prognosis of
943 colorectal cancer patients. *Mol. Oncol.* **8**, 1653–1666 (2014).

944 51. Miao, Y. *et al.* Next-Generation Surrogate Wnts Support Organoid Growth and
945 Deconvolute Frizzled Pleiotropy In Vivo. *Cell Stem Cell* **27**, 840-851.e6 (2020).

946 52. Bollen, Y., Post, J., Koo, B.-K. & Snippert, H. J. G. How to create state-of-the-art
947 genetic model systems: strategies for optimal CRISPR-mediated genome editing.
948 *Nucleic Acids Res.* **46**, 6435–6454 (2018).

949 53. Richardson, C. D., Ray, G. J., DeWitt, M. A., Curie, G. L. & Corn, J. E. Enhancing
950 homology-directed genome editing by catalytically active and inactive CRISPR-Cas9
951 using asymmetric donor DNA. *Nat. Biotechnol.* **34**, 339–344 (2016).

952 54. Bollen, Y. *et al.* Efficient and error-free fluorescent gene tagging in human organoids
953 without double-strand DNA cleavage. *PLoS Biol.* **20**, 1–16 (2022).

954 55. Fujii, M., Matano, M., Nanki, K. & Sato, T. Efficient genetic engineering of human
955 intestinal organoids using electroporation. *Nat. Protoc.* **10**, 1474–1485 (2015).

956 56. Brinkman, E. K., Chen, T., Amendola, M. & Van Steensel, B. Easy quantitative
957 assessment of genome editing by sequence trace decomposition. *Nucleic Acids Res.* **42**,
958 1–8 (2014).

959 57. Brinkman, E. K. *et al.* Easy quantification of template-directed CRISPR/Cas9 editing.
960 *Nucleic Acids Res.* **46**, e58 (2018).

961 58. Li, H. & Durbin, R. Fast and accurate long-read alignment with Burrows-Wheeler
962 transform. *Bioinformatics* **26**, 589–595 (2010).

963 59. Tarasov, A., Vilella, A. J., Cuppen, E., Nijman, I. J. & Prins, P. Sambamba: Fast
964 processing of NGS alignment formats. *Bioinformatics* **31**, 2032–2034 (2015).

965 60. McKenna, A. *et al.* The Genome Analysis Toolkit: A MapReduce framework for
966 analyzing next-generation DNA sequencing data. *Genome Res.* **20**, 1297–1303 (2010).

967 61. Boeva, V. *et al.* Control-FREEC: A tool for assessing copy number and allelic content
968 using next-generation sequencing data. *Bioinformatics* **28**, 423–425 (2012).

969 62. Cingolani, P. *et al.* Using Drosophila melanogaster as a model for genotoxic chemical
970 mutational studies with a new program, SnpSift. *Front. Genet.* **3**, 1–9 (2012).

971 63. Cingolani, P. *et al.* A program for annotating and predicting the effects of single
972 nucleotide polymorphisms, SnpEff: SNPs in the genome of Drosophila melanogaster
973 strain w1118; iso-2; iso-3. *Fly (Austin).* **6**, 80–92 (2012).

974 64. Gu, Z., Eils, R. & Schlesner, M. Complex heatmaps reveal patterns and correlations in
975 multidimensional genomic data. *Bioinformatics* **32**, 2847–2849 (2016).

976 65. Shale, C. *et al.* Unscrambling cancer genomes via integrated analysis of structural
977 variation and copy number. *Cell Genomics* **2**, 100112 (2022).

978 66. Bankhead, P. *et al.* QuPath: Open source software for digital pathology image analysis.
979 *Sci. Rep.* **7**, 1–7 (2017).

980 67. Dobin, A. *et al.* STAR: Ultrafast universal RNA-seq aligner. *Bioinformatics* **29**, 15–21
981 (2013).

982 68. Love, M. I., Huber, W. & Anders, S. Moderated estimation of fold change and
983 dispersion for RNA-seq data with DESeq2. *Genome Biol.* **15**, 1–21 (2014).

984 69. Muraro, M. J. *et al.* A Single-Cell Transcriptome Atlas of the Human Pancreas. *Cell*
985 *Syst.* **3**, 385-394.e3 (2016).

986 70. Hao, Y. *et al.* Integrated analysis of multimodal single-cell data. *Cell* **184**, 3573-
987 3587.e29 (2021).

988 71. Chen, E. Y. *et al.* Enrichr: interactive and collaborative HTML5 gene list enrichment

989 analysis tool. *BMC Bioinformatics* **14**, 128 (2013).

990 72. Korsunsky, I. *et al.* Fast, sensitive and accurate integration of single-cell data with
991 Harmony. *Nat. Methods* **16**, 1289–1296 (2019).

992 73. Guinney, J. *et al.* The consensus molecular subtypes of colorectal cancer. *Nat. Med.* **21**,
993 1350–1356 (2015).

994 74. Schmidt, U., Weigert, M., Broaddus, C. & Myers, G. Cell Detection with Star-Convex
995 Polygons. in (eds. Frangi, A. F., Schnabel, J. A., Davatzikos, C., Alberola-López, C. &
996 Fichtinger, G.) 265–273 (Springer International Publishing, 2018). doi:10.1007/978-3-
997 030-00934-2_30

998 75. Bolhaqueiro, A. C. F. *et al.* Live imaging of cell division in 3D stem-cell organoid
999 cultures. *Methods Cell Biol.* **145**, 91–106 (2018).

1000

1001

Acknowledgements

The authors thank members of the Maurice laboratory for helpful discussions and suggestions. We thank Bas Ponsioen for help with time-lapse image analysis. This work is part of the Oncode Institute, which is partly financed by the Dutch Cancer Society. This work was supported by the Netherlands Organization for Scientific Research NWO VICI Grant 91815604 (to M.M.M) and ZonMW TOP Grant 91218050 (to M.M.M., O.K. and H.J.G.S.), the IMAGINE! Gravitation grant 024.005.009 (to M.M.M. and H.J.G.S.), and Dutch Cancer Society Young Investigator Grant 11491/2018-1 (to S.J.E.S.).

Author Contributions

J.M.B., L.E.B., E.K., H.J.G.S., O.K. and M.M.M. conceptualized the project. J.M.B., O.K. and M.M.M. designed and interpreted experimental results. J.M.B. generated CRISPR lines, performed all *in vitro* organoids experiments and analysed single-cell and bulk RNAseq data, E.K. performed *in vivo* transplantation experiments and immunohistochemistry, L.E.B. prepared the PDO panel for RNAseq (Extended Data Fig. 1c), Y.H. and S.T., provided and analysed single-cell RNAseq patient data, J.S. designed and cloned the TINC-reporter construct and advised on single cell RNAseq analysis. I.J. performed FACS sorting and helped with image processing and analysis. N.F. designed the CRISPR strategy for *RNF43* correction and performed C59 experiments. D.M.G. and R.V.B. analysed and interpreted genomics data. S.J.E.S. performed time-lapse imaging and advised on hybrid co-culture experiments. J.M.B. and M.M.M. wrote the manuscript, which was reviewed by all authors.

Competing Interests

Madelon Maurice is cofounder and shareholder of Laigo Bio B.V. The other authors declare no competing interests.

1026 **Supplementary table 1: primers used for genotyping and Sanger sequencing**

RNF43_P441_fw	AAATGGCTGAGGGGAGGTTTAG
RNF43_P441_rev	AGGGAGCTGCAGAAAGTAGAAC
APC_fw	TGTAATCAGACGACACAGGAAGCAGA
APC_rev	TGGACCCTCTGAACTGCAGCAT
NDRG1_reporter_internal_fw	GGGCTGTCCCTGATATCAAACAT
NDRG1_reporter_internal_rev	CAGATCCCATACAATGGGGTAC
NDRG1_reporter_upstream_fw	TCTTTGGGAGAGATGACAACGA
NDRG1_reporter_downstream_rev	CCTGCTTTTGCTGCACATTAAG

1027

1028 **Supplementary table 2: RT-qPCR primers**

GAPDH	CTTTTGCGTCGCCAG	TTGATGGCAACAATATCCAC
AXIN2	AAAGAGAGGAGGTTCAGATG	CTGAGTCTGGGAATTTTTCTTC
RNF43	TGTGTACAAGAACCAAAAGG	CAGGATGATCACAAAGATGG
ZNRF3	CATCCTCCTTGTCAAAATCAAG	TTCTGGTTTCCATCTTCTCTAG
LGR5	AAATGCCTTATGCTTACCAG	ATCTTGAGCCTGAAACATTC
ASCL2	CGTGAAGCTGGTGAACTTGG	GGATGTACTCCACGGCTGAG

1029

1030 **Supplementary video 1:** Time-lapse series of 3D reconstructed pure RC2 H2B-mNeon
1031 organoid in growth factor depleted medium, representative image related to Fig. 2i, j.

1032 **Supplementary video 2:** Time-lapse series of 3D reconstructed RC2 H2B-mNeon organoid in
1033 hybrid structure with HUB040 H2B-mcherry in growth factor depleted medium, representative
1034 image related to Fig. 2i, j.